CHEMISTRY
A EUROPEAN JOURNAL

DOI: 10.1002/chem.200901526

Effect of CO on the Oxidative Addition of Arene C–H Bonds by Cationic Rhodium Complexes

Michael Montag,[a] Irena Efremenko,[a] Revital Cohen,[a] Linda J. W. Shimon,[b] Gregory Leitus,[b] Yael Diskin-Posner,[b] Yehoshoa Ben-David,[a] Hiyam Salem,[a] Jan M. L. Martin,*[a] and David Milstein*[a]

Dedicated to Professor Yitzhak Apeloig on the occasion of his 65th birthday

Abstract: Sequential addition of CO molecules to cationic aryl–hydrido Rh^{III} complexes of phosphine-based (PCP) pincer ligands was found to lead first to C–H reductive elimination and then to C–H oxidative addition, thereby demonstrating a dual role of CO. DFT calculations indicate that the oxidative addition reaction is directly promoted by CO, in contrast to the commonly accepted view that CO hinders such reactions. This intriguing effect was traced to repulsive π interactions along the aryl-Rh-CO axis, which are augmented by the initially added CO ligand (due to antibonding interactions between occupied Rh d_π orbitals and occupied π orbitals of both CO and the arene moiety), but counteracted by the second CO ligand (due to significant π back-donation). These repulsive interactions were themselves linked to significant weakening of the π-acceptor character of CO in the positively charged rhodium complexes, which is concurrent with an enhanced σ-donating capability. Replacement of the phosphine ligands by an analogous phosphinite-based (POCOP) pincer ligand led to significant changes in reactivity, whereby addition of CO did not result in C–H reductive elimination, but yielded relatively stable mono- and dicarbonyl aryl–hydrido POCOP–Rh^{III} complexes. DFT calculations showed that the stability of these complexes arises from the higher electrophilicity of the POCOP ligand, relative to PCP, which leads to partial reduction of the excessive π-electron density along the aryl-Rh-CO axis. Finally, comparison between the effects of CO and acetonitrile on C–H oxidative addition revealed that they exhibit similar reactivity, despite their markedly different electronic properties. However, DFT calculations indicate that the two ligands operate by different mechanisms.

Keywords: carbon monoxide · C–H activation · density functional calculations · oxidative addition · rhodium

Introduction

The activation of strong carbon–hydrogen bonds by transition metals is one of the fundamental fields of current organometallic chemistry. The ability to selectively cleave and functionalize otherwise inert C–H bonds, such as those in alkanes or arenes, and to do so under mild conditions, would pave the way to a more cost-effective utilization of abundant chemical feedstocks, such as oil and natural gas. To this end, it is crucial to further our understanding of the underlying processes involved in C–H bond activation.

Cleavage of C–H bonds by transition metals may take place through several possible pathways that are generally dependant on the electron density at the metal center.[1] For electron-rich, low-valent transition metals, the typical pathway for C–H cleavage is oxidative addition, thus leading to the corresponding alkyl– or aryl–hydrido complexes, with a concomitant formal two-electron oxidation of the metal.[2] Transition metals that lack the electron density necessary to undergo oxidative addition, such as early transition metals

[a] Dr. M. Montag, Dr. I. Efremenko, Dr. R. Cohen, Y. Ben-David, Dr. H. Salem, Prof. J. M. L. Martin, Prof. D. Milstein
Department of Organic Chemistry
Weizmann Institute of Science, Rehovot 76000 (Israel)
Fax: (+972) 8-934-4142
E-mail: gershom@weizmann.ac.il
david.milstein@weizmann.ac.il

[b] Dr. L. J. W. Shimon, Dr. G. Leitus, Dr. Y. Diskin-Posner
Department of Chemical Research Support
Weizmann Institute of Science, Rehovot 76000 (Israel)

Supporting information for this article is available on the WWW under http://dx.doi.org/10.1002/chem.200901526.

or high-valent late transition metals, may activate C–H bonds through alternative routes, namely, σ-bond metathesis, radical activation, 1,2-addition, and electrophilic substitution.[1] It is widely accepted that both σ-bond metathesis and oxidative addition processes take place through σ complexes or agostic intermediates.[3]

According to the classic work of Saillard and Hoffmann,[4] oxidative addition of a C–H bond to a transition-metal center involves a two-way electron transfer, that is, from the filled σ orbital of the C–H bond into an empty metal d orbital, and from a filled metal d orbital into the empty σ* orbital of the C–H bond. However, these electron transfers do not balance out and this results in a net transfer of electron density from the metal to the C–H bond (which splits into formally anionic hydrocarbyl and hydride ligands). Therefore, the presence of electron-withdrawing ligands, such as the strong π-acceptor ligand carbon monoxide, would be expected to hinder oxidative addition and to facilitate reductive elimination of C–H bonds by lowering the electron density at the metal center.[5,6]

In a recent communication, we have reported on a series of cationic rhodium complexes that were based on pincer-type bisphosphine ligand **1** (Scheme 1), and which yielded

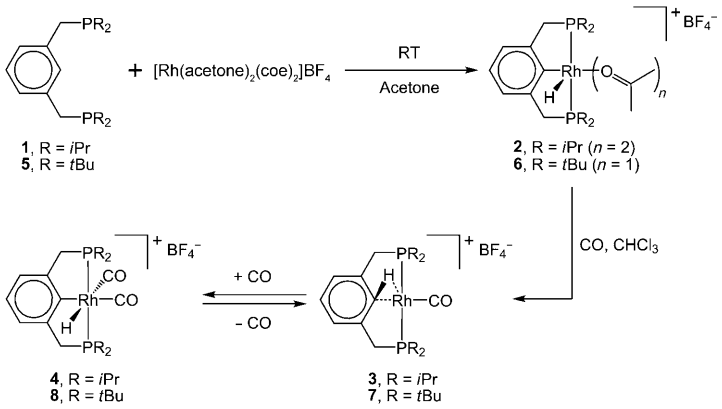

Scheme 1. Preparation of PCP–Rh^{III} complexes **2** and **6**, and their reactions with CO.

intriguing observations regarding the effect of CO on the activation of C–H bonds.[7] Thus, it had been found that when Rh^{III} aryl–hydrido complex **2** was treated with one equivalent of CO, facile C–H reductive elimination took place, as expected, to yield agostic Rh^{I} complex **3**. However, when a second equivalent of CO was added to this system, facile oxidative addition of the same C–H bond took place, thereby yielding Rh^{III} aryl–hydrido complex **4**. Both experimental and theoretical evidence indicated that this oxidative addition reaction was actually promoted by CO, which did not merely act as a trapping agent.

In the current report we present further experimental evidence regarding this intriguing dual effect of CO. We shall examine the effect of different pincer ligands, and will also compare the behavior of CO to that of the strong σ-donor acetonitrile. The new results are augmented by rigorous theoretical calculations, which further demonstrates the versatile nature of CO as both a σ-donor and π-acceptor ligand.

Results and Discussion

Preparation and structure of cationic, solvent-stabilized, aryl–hydrido PCP-type pincer complexes of Rh^{III}: In our previous communication, we described the reaction of the solvent-stabilized, aryl–hydrido complex **2** with CO.[7] Complex **2** was prepared by reacting the cationic Rh^{I} precursor $[Rh(acetone)_2(coe)_2]BF_4$ (coe = cyclooctene) with one equivalent of the isopropyl-substituted, phosphine-based pincer ligand **1** (see Scheme 1). Thus, when solutions of $[Rh(acetone)_2(coe)_2]BF_4$ and ligand **1** in acetone were mixed at room temperature, a rapid reaction took place that involved C–H bond cleavage and afforded complex **2** in very high yield. In the present work, we employed the same technique, using the bulkier, *tert*-butyl-substituted ligand **5**, to prepare a more sterically constrained analogue of complex **2**, namely, complex **6**. The reaction of **5** with $[Rh(acetone)_2(coe)_2]BF_4$ in acetone was also found to be very facile and resulted in a high yield of complex **6**.

The $^{31}P\{^1H\}$ NMR spectrum of complex **6** in $CDCl_3$ exhibited a doublet at $\delta = 77.51$ ppm ($^1J(Rh,P) = 115.9$ Hz), and its ^1H NMR spectrum contained a characteristic hydride signal at $\delta = -27.48$ ppm (doublet-of-triplets, $^1J(Rh,H) = 59.0$ Hz, $^2J(P,H) = 10.8$ Hz). Such a high-field hydride signal is characteristic of a hydride ligand *trans* to a vacant coordination site, or to a loosely coordinated ligand, such as the solvent or BF_4^- counterion. Full characterization of this complex, including X-ray crystallography (see below), revealed a molecular structure that is analogous to the previously reported complex **2**, as shown in Scheme 1.

Crystals of complex **6** suitable for X-ray diffraction were grown at room temperature from a solution of **6** in acetone/dichloromethane overlaid with pentane (see Table 1 for the crystallographic parameters). This complex was found to crystallize in the $P2_1/c$ space group, with each asymmetric unit being comprised of a single cationic complex and a non-coordinated BF_4^- counterion. The cationic fragment, which is shown in Figure 1, features a pentacoordinate rhodium atom centered at the base of a distorted square-pyramidal coordination geometry, in which the equatorial positions are occupied by the pincer ligand and an acetone molecule (*trans* to the aryl *ipso* carbon), while the axial position is occupied by the hydride ligand.[8,9] This structural arrangement is consistent with the conclusions drawn from the solution NMR spectra of **6** (i.e., hydride ligand *trans* to a vacant site), and also bears great similarity to the crystal structure of complex **2**, as previously reported.[7] Selected bond lengths and angles for complex **6** are presented in Table 2.

It is worth noting that although complex **6** bears a pentacoordinate rhodium center in the crystal structure, with only one coordinated solvent molecule and an outer-sphere BF_4^- counterion, this is not necessarily the case in solution. Firstly, the ^1H NMR chemical shift of the hydride signal was

Table 1. Crystallographic data for complexes **6**, **14**, **16**, and **17**.

	6	**14**	**16**	**17**
formula	$C_{27}H_{50}OP_2Rh{\cdot}BF_4$	$C_{25}H_{46}O_3P_2Rh{\cdot}BF_4$	$C_{24}H_{39}O_4P_2Rh{\cdot}2\,BF_4{\cdot}CH_2Cl_2$	$C_{23}H_{39}O_3P_2Rh$
crystal description	yellow prism	yellow chunk	yellow plate	yellow prism
crystal size [mm^3]	$0.20\times0.20\times0.18$	$0.35\times0.25\times0.10$	$0.30\times0.20\times0.05$	$0.30\times0.30\times0.20$
M_r [g mol^{-1}]	642.33	646.28	814.95	528.39
space group	$P2_1/c$	$P2_1/c$	$C2/c$	$P\bar{1}$
crystal system	monoclinic	monoclinic	monoclinic	triclinic
a [Å]	12.0273(2)	14.8893(3)	23.4810(3)	8.2830(17)
b [Å]	14.9999(4)	29.9575(6)	12.5590(4)	12.058(2)
c [Å]	17.5734(4)	13.2879(2)	24.7290(8)	13.434(3)
α [°]	90.00	90.00	90.00	100.62(3)
β [°]	92.3385(13)	96.0619(9)	107.0790(17)	96.13(3)
γ [°]	90.00	90.00	90.00	103.91(2)
V [Å^3]	3167.75(12)	5893.88(19)	6970.9(3)	1263.9(5)
Z	4	8	8	2
ρ_{calcd} [g cm^{-3}]	1.347	1.457	1.553	1.388
μ [mm^{-1}]	0.681	0.738	0.807	0.822
reflns	30036	52967	45781	23982
unique reflns	11373	14914	15364	5725
$2\theta_{max}$ [°]	59.14	54.2	50.7	54.96
R_{int}	0.062	0.060	0.058	0.042
params (restraints)	400 (20)	679 (0)	406 (0)	274 (0)
final R ($I>2\sigma(I)$)	0.0540	0.0400	0.0670	0.0382
wR ($I>2\sigma(I)$)	0.1412	0.0964	0.1416	0.0916
GOF	1.086	1.035	1.115	1.056

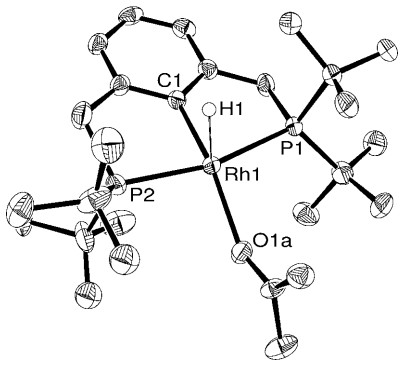

Figure 1. ORTEP drawing of complex **6** (50% probability level). Hydrogen atoms (except for hydride) and the BF_4^- counterion have been omitted for clarity. It should be noted that this crystal structure was found to be disordered with respect to the acetone ligand and the *tert*-butyl substituents on P2. Only one of the possible configurations is shown here.

Table 2. Selected bond lengths [Å] and angles [°] for complex **6**.[a]

Rh1–C1	2.009(3)	Rh1–P1	2.3295(8)
Rh1–O1a	2.163(4)	Rh1–P2	2.3195(8)
Rh1–O1b	2.197(6)		
C1-Rh1-P1	83.07(9)	O1b-Rh1-P2	101.46(16)
C1-Rh1-P2	83.47(9)	C1-Rh1-O1a	162.36(15)
O1a-Rh1-P1	99.60(9)	C1-Rh1-O1b	167.9(2)
O1b-Rh1-P1	91.18(16)	P1-Rh1-P2	166.19(3)
O1a-Rh1-P2	94.16(9)		

[a] The acetone ligand in **6** exhibits disorder, and its oxygen atom (O1) appears in two positions, both of which are included in this table (O1a, O1b).

found to vary significantly with the solvent, such that in $CDCl_3$ this signal appears at $\delta=-27.48$ ppm, whereas in [D$_6$]acetone it appears at $\delta=-22.84$ ppm (broad doublet, ^1J(Rh,H) = 34.0 Hz), which is over 4.6 ppm downfield.[10] Secondly, the $^{19}F\{^1H\}$ NMR spectrum of complex **6** in $CDCl_3$ features an extremely broad BF_4^- signal at $\delta=-167.0$ ppm ($\Delta\nu_{1/2}\approx1800$ Hz), which clearly indicates that in this solvent the BF_4^- counterion is coordinated to the metal center, albeit in a fluxional manner that leads to a broad NMR signal.

Addition of CO to complexes 2 and 6 and formation of C–H agostic and aryl–hydrido complexes: As previously communicated,[7] when a solution of the *i*Pr-substituted complex **2** in chloroform was treated with excess CO, a mixture of two products was obtained, comprised of the agostic monocarbonyl complex **3** and the aryl–hydrido dicarbonyl complex **4** (Scheme 1). Because of the facile equilibrium between these two complexes, with participation of the sparingly soluble CO, their room-temperature ^1H and ^{31}P NMR spectra featured extremely broad signals that became well-resolved only upon cooling to −55 °C. In order to examine the behavior of the *t*Bu-substituted system under the same conditions, a solution of **6** in chloroform was also treated with excess CO. The $^{31}P\{^1H\}$ NMR spectrum of the resulting solution at room temperature was found to exhibit a single, well-defined doublet at $\delta=35.40$ ppm (^1J(Rh,P) = 100.3 Hz), and no hydride signals were observed in its ^1H NMR spectrum. Further examination of the NMR data confirmed that the sole observable product of this reaction was the agostic complex **7** (see Scheme 1), which was previously reported by our group.[11] The fact that this was the only product observed at room temperature is in marked contrast to the results obtained with the *i*Pr-substituted system, as described above. Nonetheless, examination of the ^1H and ^{31}P NMR spectra of the solution containing complex **7**, after the

excess CO had been pumped off, revealed slight yet noticeable line narrowing, as compared with the spectra measured under excess CO (for example, the ^{31}P NMR signal linewidth changed from 17 to 6 Hz). This observation raised the possibility that complex **7** is engaged in a fluxional process involving CO, as was previously observed for the *i*Pr-substituted system (**3**+CO⇄**4**). Indeed, when a solution of **7** in chloroform was cooled to −40 °C under excess CO, a second product was observed. The new product gave rise to a doublet at $\delta = 98.13$ ppm ($^1J(Rh,P) = 89.9$ Hz) in the $^{31}P\{^1H\}$ NMR spectrum, as well as a hydride signal at $\delta = -8.95$ ppm (doublet-of-triplets, $^1J(Rh,H) = 11.6$ Hz, $^2J(P,H) = 3.5$ Hz) in the ^1H NMR spectrum. Moreover, the $^{13}C\{^1H\}$ NMR spectrum of this complex featured two carbonyl signals at $\delta = 186.86$ ppm (multiplet, $^1J(Rh,C) = 40.7$ Hz) and $\delta = 185.59$ ppm (doublet-of-triplets, $^1J(Rh,C) = 42.8$ Hz, $^2J(P,C) = 9.2$ Hz), which are consistent with the existence of two magnetically nonequivalent carbonyl ligands. Full characterization of this compound revealed it to be complex **8** (see Scheme 1), the *tert*-butyl analogue of previously reported complex **4**.

It should be noted that the precise configuration of the carbonyl ligands in **8** was verified by using ^{13}C-labeled CO and noting the effects of this isotope labeling on the observed coupling constants of the ^1H, ^{13}C, and ^{31}P NMR signals.[12] Thus, the incorporation of ^{13}CO led to the appearance of an additional double-doublet splitting in the $^{31}P\{^1H\}$ NMR signal for complex **8** ($^2J(C,P) = 9.0$ Hz, 6.3 Hz), thereby verifying the existence of two CO ligands. Furthermore, the hydride signal in the ^1H NMR spectrum of this complex exhibited a large $^1H,^{13}C$ coupling constant of 59.6 Hz, which was also observed for the carbonyl ^{13}C NMR signal at $\delta = 186.86$ ppm, and this indicated that these two ligands are in a *trans* configuration.[13] The second CO ligand ($\delta(^{13}C) = 185.59$ ppm) exhibited a much smaller $^1H,^{13}C$ coupling constant of 4.8 Hz, and this indicated that it is positioned *cis* to the hydride.[13] Moreover, no $^{13}C,^{13}C$ coupling between the two CO ligands was observed, which is consistent with a *cis* configuration for these ligands.[14]

The reaction between complex **7** and CO to yield complex **8** was found to be highly reversible, as was previously observed for complexes **3** and **4**. Thus, when a solution of **7** in dichloromethane was cooled to −60 °C under excess CO, it was found to initially contain a mixture of **7** and **8**, with **7** being the more abundant species (**7**:**8**≈2:1, based on integration of the ^{31}P NMR signals). However, when this solution was re-examined after being kept for 11 h at −60 °C, complex **8** was found to be much more abundant than **7** (**7**/**8** ≈1:3). Nonetheless, upon warming the solution to room temperature, complex **8** all but disappeared, leaving complex **7** as the only observed species in solution.[15] Further evidence for the reversibility of this process was obtained by ^1H NMR spectroscopy spin saturation transfer (SST) experiments carried out at various temperatures, chosen such that both complexes **7** and **8** were observable (≤0 °C). During these experiments, the hydride ligand in complex **8** was selectively irradiated in the NMR spectrometer, and this led to a reduction in the intensity of the signal associated with the agostic proton in **7**, thus providing direct evidence for a chemical exchange between the two sites (see the Experimental Section).[16] These experiments unequivocally showed that complexes **7** and **8** are in dynamic equilibrium at temperatures as low as −50 °C. Such a facile dynamic equilibrium was also observed for the previously described isopropyl system (**3**+CO⇄**4**) using the same method.

The above results clearly show that both the *i*Pr- and *t*Bu-substituted systems exhibit a dual role for CO. Thus, the first molecule of CO adds to the Rh^{III} aryl–hydrido–solvento complexes (**2** or **6**), and this brings about C–H reductive elimination and formation of the agostic monocarbonyl Rh^I complexes (**3** or **7**). The second molecule of CO then adds to the latter complex and this leads to oxidative addition of the same C–H bond and formation of the aryl–hydrido–dicarbonyl Rh^{III} complexes (**4** or **8**). The only qualitatively noticeable difference between the *i*Pr- and *t*Bu-substituted systems is the fact that complex **7** exhibits no significant reaction under excess CO at room temperature, whereas complex **3** reacts completely with CO to give complex **4**.[7]

Mechanism of C–H oxidative addition under CO—A DFT examination: The promotion of C–H reductive elimination by CO, as observed for complexes **2** and **6**, is entirely consistent with the commonly accepted view of CO as a strong π-acceptor ligand, with a relatively weak capacity for σ donation. Thus, the coordinated CO molecule is expected to reduce the electron density on the Rh^{III} center of either **2** or **6**, thereby leading to the elimination of the C–H bond, with concomitant formal reduction of the metal to Rh^I and formation of the agostic complexes. On the other hand, the fact that further addition of CO to the Rh^I agostic complexes (**3** and **7**) leads to oxidative addition of the agostic C–H bond, with formation of the corresponding aryl–hydrido Rh^{III} complexes (**4** and **8**, respectively), is highly unusual and counterintuitive, as it contradicts the expected classical role of CO.

In order to account for the seemingly contradictory roles of CO, it was first necessary to probe the underlying reaction mechanisms. The experimental observations described above prompted us to propose two alternative mechanistic pathways for the reaction between CO and the agostic complexes, as shown in Scheme 2. In the first pathway (A), the agostic Rh^I complex (**3** or **7**) undergoes spontaneous C–H oxidative addition to yield a square-pyramidal aryl–hydrido–monocarbonyl Rh^{III} intermediate (**9** or **11**). This intermediate is then trapped by an incoming CO molecule to afford the aryl–hydrido–dicarbonyl Rh^{III} product (**4** or **8**). In the second pathway (B), the agostic complex reacts directly with a molecule of CO to afford an agostic-like trigonal-bipyramidal dicarbonyl Rh^I intermediate (**10** or **12**). This intermediate then undergoes C–H oxidative addition to give the aryl–hydrido–dicarbonyl product. All of the suggested reaction steps were deemed reversible, in order to account for the experimentally observed reversibility of the overall process in both the *i*Pr- and *t*Bu-substituted systems.

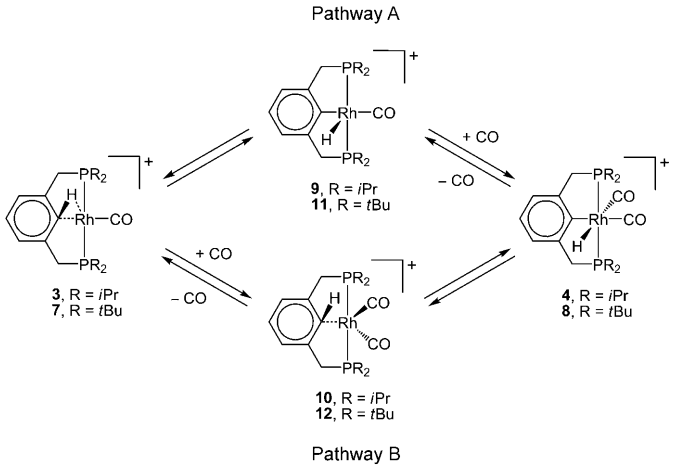

Scheme 2. Proposed reaction pathways for the agostic/aryl–hydrido equilibrium. The BF_4^- counterion has been omitted for clarity.

Neither solvent molecules nor the BF_4^- counterion were explicitly implicated in the suggested reaction pathways. Solvent coordination was assumed to be negligible, since chloroform, which is the primary solvent used in the current work, is widely known to be a very weak ligand.[17] Moreover, small amounts of acetone, which are released into the solution when complexes **2** or **6** react with CO to afford the agostic complexes, were also excluded from the proposed mechanisms, since no coordination of acetone was found by variable temperature ^{1}H NMR experiments. Regarding the BF_4^- counterion, variable temperature ^{19}F NMR experiments gave no indication for its coordination to the rhodium complexes, since no significant coordination-induced chemical shifts or line broadenings were observed.[18]

The experimental examination of the proposed reaction pathways was hampered by the fact that none of the suggested intermediates (**9**–**12**) were directly observed by variable-temperature NMR spectroscopy. Therefore, we undertook a density functional theory (DFT) study to probe and compare the two reaction pathways.[19] This computational examination was carried out using the PBE0 hybrid functional in combination with the SDB-cc-pVDZ basis set. No structural simplifications were employed in the study, and geometry optimizations were carried out on the complete complex structures, as shown in Scheme 2. Bulk solvent effects were approximated by using a conductor-like screening model (COSMO) with chloroform as the solvent. Selected optimized geometric parameters for all complexes, together with computed natural charges on the CO ligands, are listed in Table 3. It is noteworthy that the optimized geometries of complexes **3** and **7** are in excellent agreement with their previously reported crystal-structure data,[7,11a] which corroborates the accuracy of the computational methodology used in the present work. For more details regarding this methodology, see the Experimental Section.

The data in Table 3 clearly show that the computed structures of the Rh^{III} aryl–hydrido complexes (**4**, **8**, **9**, and **11**) bear longer Rh–CO bonds and shorter C–O bonds than the agostic Rh^{I} complexes (**3**, **7**, **10**, and **12**). These differences in bond lengths are in line with the classical notion that a higher oxidation state entails smaller Rh→CO π back-donation. Furthermore, in each of the dicarbonyl complexes (**4**, **8**, **10**, and **12**), the two CO ligands are found to be nonequivalent in terms of bond lengths, with the CO ligand *trans* to

Table 3. Selected optimized interatomic distances [Å], angles [°], and total natural charges (Q) on CO ligands for the PCP–rhodium complexes shown in Scheme 2.[a]

*i*Pr-substituted systems	**3**	**4**	**TS(3–9)**	**9**	**TS(10–4)**	**10**
Rh–P1	2.340	2.355	2.333	2.334	2.360	2.382
Rh–P2	2.340	2.366	2.333	2.336	2.357	2.386
Rh–C_{ipso}	2.256	2.094	2.061	2.049	2.143	2.514
C_{ipso}–H	1.137	2.435	1.736	2.468	1.464	1.103
Rh–H	1.911	1.573	1.544	1.502	1.629	2.345
Rh–C (CO_{trans})	1.826	1.939	1.917	1.934	1.926	1.873
Rh–C (CO_{cis})	–	1.978	–	–	1.985	1.895
C–O (CO_{trans})	1.150	1.139	1.144	1.141	1.143	1.150
C–O (CO_{cis})	–	1.137	–	–	1.141	1.148
∢OC_{trans}-Rh-C_{ipso}	177.0	168.6	170.3	177.6	154.9	119.7
∢Rh-C_{trans}-O	178.2	175.1	173.3	176.4	178.7	167.8
∢OC_{cis}-Rh-C_{ipso}	–	93.2	–	–	101.1	112.7
∢Rh-C_{cis}-O	–	179.2	–	–	178.0	166.0
∢Rh-C_{ipso}-C_{para}	137.9	179.4	168.3	176.0	170.7	120.4
Q(CO_{trans})	0.246	0.296	0.375	0.279	0.396	0.056
Q(CO_{cis})	–	0.225	–	–	0.375	0.057
*t*Bu-substituted systems	**7**	**8**	**TS(7–11)**	**11**	**TS(12–8)**	**12**
Rh–P1	2.358	2.381	2.350	2.347	2.386	2.420
Rh–P2	2.358	2.386	2.350	2.363	2.386	2.420
Rh–C_{ipso}	2.256	2.087	2.067	2.057	2.135	2.528
C_{ipso}–H	1.139	2.461	1.684	2.486	1.440	1.101
Rh–H	1.890	1.563	1.542	1.502	1.622	2.448
Rh–C (CO_{trans})	1.824	1.939	1.915	1.929	1.912	1.841
Rh–C (CO_{cis})	–	1.978	–	–	1.995	1.931
C–O (CO_{trans})	1.151	1.140	1.145	1.143	1.145	1.154
C–O (CO_{cis})	–	1.138	–	–	1.141	1.148
∢OC_{trans}-Rh-C_{ipso}	176.6	173.0	170.4	177.4	163.6	137.7
∢Rh-C_{trans}-O	177.8	177.2	174.7	176.7	168.7	177.4
∢OC_{cis}-Rh-C_{ipso}	–	87.4	–	–	89.4	96.6
∢Rh-C_{cis}-O	–	174.9	–	–	162.9	167.3
∢Rh-C_{ipso}-C_{para}	140.3	177.1	173.1	175.7	174.1	113.7
Q(CO_{trans})	0.235	0.303	0.350	0.279	0.362	0.056
Q(CO_{cis})	–	0.218	–	–	0.362	0.034

[a] CO_{trans} and CO_{cis} refer to the CO ligands positioned *trans* and *cis* to the C_{ipso} atom, respectively.

the aromatic ring having a shorter Rh–CO bond and a longer C–O bond than the CO ligand in the *cis* position. This indicates a stronger Rh→CO π back-donation in the CO ligands *trans* to the aryl, a conclusion that is also supported by charge decomposition analysis (CDA; see below for further details). Another noteworthy attribute of several dicarbonyl complexes (e.g., **10**, **TS(12–8)**, **12**) is their markedly bent CO ligands, as is evident from the significantly nonlinear Rh-C-O angles (see Table 3). The origin and role of this structural feature will be discussed below.

The computed energy profiles for the proposed reaction pathways of both the *i*Pr- and *t*Bu-substituted systems, at 25 and −40 °C, are shown in Figure 2. As can be seen in this figure, the energy profiles for both systems are qualitatively very similar. First and foremost, in both systems the dicarbonyl aryl–hydrido complexes (**4** and **8**) are more stable than the monocarbonyl agostic complexes (**3** and **7**). At room temperature the energy differences amount to 2.6 and 0.8 kcal mol^{-1} for the *i*Pr- and *t*Bu-substituted systems, respectively. Although these energetic differences are admittedly small, and approach the margin of error expected for DFT calculations at the present level, they do reflect the experimentally observed differences between the *i*Pr- and *t*Bu-substituted systems, whereby the former reacts completely with CO at room temperature, while the latter exhibits no appreciable reaction under the same conditions.[20] An even better agreement between the computed reaction profiles and the experimental observations was obtained when the energies were calculated for −40 °C. At this temperature, both systems exhibit greater stabilization of the aryl–hydrido products relative to their agostic precursors, by 5.3 and 3.5 kcal mol^{-1} for the *i*Pr- and *t*Bu-substituted systems, respectively. This is in line with the experimentally observed dominance of the aryl–hydrido complexes at low temperatures.

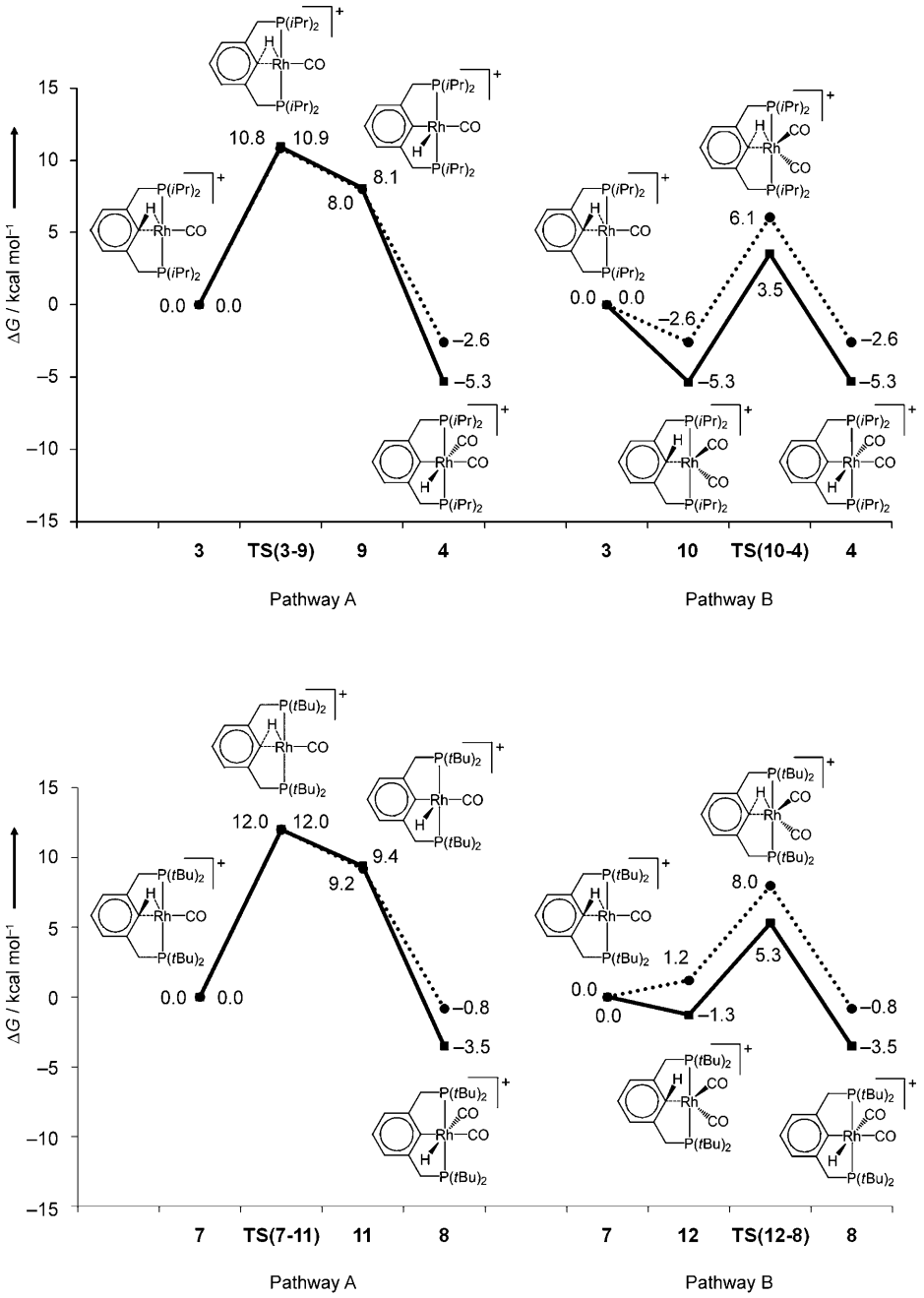

Figure 2. Calculated energy profiles of the proposed reaction pathways for the addition of CO to the cationic agostic complexes in the *i*Pr-substituted (top) and *t*Bu-substituted (bottom) systems at 25 °C (···●···) and −40 °C (——■——). The monocarbonyl agostic complex of each system (**3**, **7**) is taken as the reference energy point for that system.

A second, important attribute of the computed reaction profiles is the significantly higher stability of the trigonal-bipyramidal dicarbonyl–Rh^{I} intermediates (**10** and **12**) relative to the square-pyramidal monocarbonyl–Rh^{III} intermediates (**9** and **11**), in both the *i*Pr- and *t*Bu-substituted systems. In fact, complexes **10** and **12** were calculated to be even more stable than their corresponding agostic precursors at −40 °C,

and this was also found to be true for complex **10** at room temperature. Moreover, these intermediates were found to be very close in energy to the aryl–hydrido products, and, in the case of the *i*Pr-substituted system, the intermediate and product were found to be essentially isoenergetic. The fact that these intermediates were not directly observed experimentally, in contrast to both the agostic precursors and aryl–hydrido products, probably reflects a bias in the computational model. Nonetheless, we have found that explicitly including interactions between the cationic complexes and the BF_4^- counterion, which were hitherto neglected, resolves this apparent discrepancy, as will be discussed below.

Although neither intermediate **10** nor **12** were directly observed, indirect experimental evidence for their existence was obtained. Thus, when a solution of the cationic Rh^I precursor $[Rh(acetone)_2(CO)_2]BF_4$[21] in acetone was mixed at −78 °C with an acetone solution which contained an equimolar amount of either ligand **1** or **5**, the corresponding aryl–hydrido–dicarbonyl complexes were obtained, whereas the agostic complexes were not observed. For ligand **1**, the same result was also achieved at room temperature, as previously reported.[7] Although these reactions were not clean, and significant amounts of byproducts were observed,[22] the fact that the aryl–hydrido–dicarbonyl complexes could be prepared directly from the dicarbonyl precursor, in the absence of agostic complexes, strongly supports the involvement of the proposed trigonal-bipyramidal intermediates in both the *i*Pr- and *t*Bu-substituted systems.

Finally, and most importantly, the computed energy profiles for both the *i*Pr- and *t*Bu-substituted systems clearly indicate that pathway B is kinetically more favorable than pathway A, as it exhibits lower energy barriers. In the *i*Pr-substituted system, the kinetic barrier for pathway B is nearly 2 kcal mol^{-1} lower than that for pathway A, whereas in the *t*Bu-substituted system the preference for pathway B is even more pronounced, with its energy barriers being 4.0–5.4 kcal mol^{-1} lower than those of pathway A. Therefore, it is possible to conclude that although both reaction pathways are feasible, the oxidative addition of C–H bonds in the cationic PCP–rhodium systems is much more likely to occur through direct promotion by CO coordination.

Effect of BF_4^- on the reaction profiles: As described above, the energy profiles shown in Figure 2 are in good agreement with the experimentally observed reactivity of the PCP–rhodium complexes towards CO. Nonetheless, a few discrepancies between the theoretical model and experimental findings were identified, the most notable of which were the predicted stabilities of intermediates **10** and **12**, which were inconsistent with the fact that they had not been observed experimentally. This discrepancy prompted us to investigate the possible effect of the BF_4^- counterion, which was hitherto excluded from the DFT study. In general, even though BF_4^- has a very low capacity for covalent interactions, its ionic interactions with the cationic complexes may be quite significant, especially in nonpolar media such as chloroform. This, in turn, may affect the overall energy balance of the studied systems, especially in light of the small energy differences involved.

Two types of interactions between BF_4^- and the carbonyl complexes were addressed in our computational examination, namely, inner-sphere coordination to the metal center (only in the monocarbonyl complexes where this is sterically feasible) and outer-sphere interaction with the agostic proton or hydride ligand (in all complexes).[23] The computed free energies for BF_4^- binding in $CHCl_3$, at 25 and −40 °C, are listed in Table 4. All ground-state complexes, in both the *i*Pr- and *t*Bu-substituted systems, were found to exhibit a thermodynamically favorable interaction between BF_4^- and either the agostic proton or hydride ligand, whereas coordination to the metal center was generally found to be unfavorable. Interestingly, the only exception was found to be intermediate **11**, in which coordination of BF_4^- to the metal center was found to be more stabilizing than its interaction with the hydride ligand. All transition states associated with the *i*Pr-substituted system were found to be stabilized by BF_4^-, regardless of the mode of interaction, whereas in the *t*Bu-substituted system the transition states exhibit mostly destabilizing interactions with BF_4^-.

Table 4. Computed free energies for BF_4^- interaction with *i*Pr- and *t*Bu-substituted PCP-rhodium complexes in $CHCl_3$ at 25 and −40 °C (values are in kcal mol^{-1}).[a]

*i*Pr-substituted	*T* [°C]		*t*Bu-substituted	*T* [°C]	
	25	−40		25	−40
3-BF_4^H	−2.85	−5.23	**7**-BF_4^H	−5.29	−7.83
3-BF_4^{Rh}	3.19	0.71	**7**-BF_4^{Rh}	0.45	0.63
4-BF_4^H	−4.16	−6.55	**8**-BF_4^H	−2.67	−5.5
9-BF_4^H	−2.30	−5.01	**11**-BF_4^H	−0.58	−3.84
9-BF_4^{Rh}	2.48	−0.61	**11**-BF_4^{Rh}	−6.74	−9.69
10-BF_4^H	−0.86	−3.12	**12**-BF_4^H	−1.15	−3.98
TS(3–9)-BF_4^{Rh}	−4.46	−7.62	**TS(7–11)**-BF_4^{Rh}	0.82	−2.11
TS(3–9)-BF_4^H	−4.45	−7.40	**TS(7–11)**-BF_4^H	5.8[b]	2.8[b]
TS(10–4)-BF_4^H	−2.64	−5.21	**TS(12–8)**-BF_4^H	4.3[b]	1.7[b]

[a] The superscript H indicates interaction of BF_4^- with either the agostic proton or hydride ligand; the superscript Rh indicates coordination to the metal center. [b] These energies were estimated using relaxed scans of the potential-energy surface near the critical point (see ref. [24]).

The effects of BF_4^- on the relative stabilities of the various species along the proposed reaction pathways result in significant changes in these pathways. The modified reaction profiles are shown in Figure 3. As can be seen in this figure, the inclusion of BF_4^- allows for two alternative versions of pathway A, depending on the mode of interaction between BF_4^- and the different complexes. In pathway A_1, both the mono- and dicarbonyl species experience outer-sphere interactions with the BF_4^- counterion, through the agostic proton or hydride ligand. In pathway A_2, on the other hand, the monocarbonyl species interact with BF_4^- through inner-sphere coordination, whereas the dicarbonyl complex interacts with the counterion through the hydride ligand (since metal coordination is not possible). It is worth noting that the latter pathway requires BF_4^- to detach from the metal center of complex **9** or **11** prior to the coordination of a

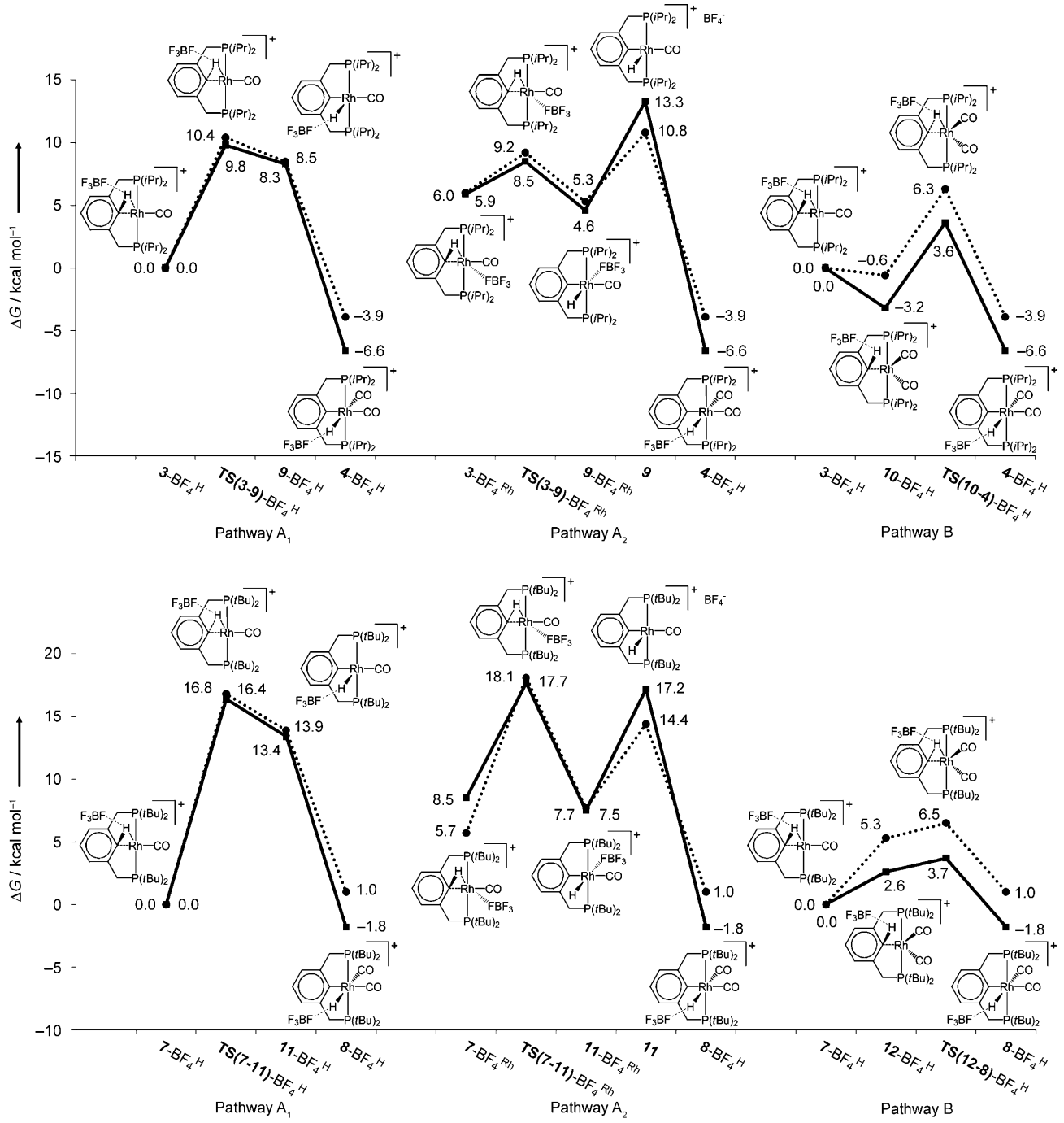

Figure 3. Calculated energy profiles of the proposed reaction pathways for the *i*Pr-substituted (top) and *t*Bu-substituted (bottom) systems in the presence of BF_4^-, at 25 °C (···●···) and −40 °C (——■——). For each system, the monocarbonyl agostic complex with BF_4^- bound to its agostic proton (**3**-BF_4^H, **7**-BF_4^H) is taken as the reference energy point for that system.

second CO molecule, thereby involving a high-energy separated-ion-pair state. Pathway B, in contrast to A, allows for only one mode of counterion binding, namely, outer-sphere interactions with the agostic proton or hydride ligand.

In the *i*Pr-substituted system, the inclusion of BF_4^- in the computed reaction profiles increases the thermodynamic driving force and decreases the activation barriers for C–H oxidative addition. The most pronounced change was found for pathway A_2, in which the inner-sphere coordination of BF_4^- affords an activation barrier of as low as 3.2 kcal mol^{-1} by destabilizing the agostic complex (**3**-BF_4^{Rh}) while stabilizing the transition state (**TS(3–9)**-BF_4^{Rh}). However, the strong destabilization of **3**-BF_4^{Rh} places it 6 kcal mol^{-1} higher in energy than agostic species **3**-BF_4^H, which indicates that the former is much less likely to occur in solution. Moreover, pathway A_2 involves the energetically unfavorable dissocia-

tion of BF_4^- as a rate-limiting step, which brings the overall kinetic barrier for this pathway to 10.8–13.3 kcal mol^{-1}. At room temperature this equals the kinetic barrier of pathway A in the absence of BF_4^-, and at low temperature it surpasses it by 2.4 kcal mol^{-1}. Pathway A_1, on the other hand, exhibits a kinetic barrier which is 0.4–1.1 kcal mol^{-1} lower than in the absence of BF_4^-, and it is also thermodynamically favored over pathway A_2. As for pathway B, it also experiences a decrease in its kinetic barrier as a result of the interaction with BF_4^-, which amounts to about 2 kcal mol^{-1} relative to the same pathway in the absence of BF_4^-. All in all, the incorporation of BF_4^- in the *i*Pr-substituted system maintains pathway B as the most likely route to C–H oxidative addition, as was previously concluded. However, in contrast to our previous results, the inclusion of BF_4^- renders aryl–hydrido complex **4** more stable than intermediate **10** by over 3 kcal mol^{-1} (at both 25 and −40 °C) while maintaining the stability of this species relative to intermediate **9** (by 5.9–11.5 kcal mol^{-1}, depending on the temperature and mode of interaction with BF_4^-). This greatly improves the agreement between the computed and experimental results, as it supports the involvement of **10** in the reaction mechanism while accounting for the fact that this intermediate was not observed experimentally.

The *t*Bu-substituted system, like its *i*Pr-substituted analogue, exhibits marked changes in the reaction profiles upon incorporation of BF_4^-, and these changes enhance the kinetic and thermodynamic preference for pathway B relative to pathways A_1 and A_2. In fact, the kinetic barrier for pathway B in the presence of BF_4^- is predicted to be as low as 3.7 kcal mol^{-1} (at −40 °C),[24] which is nearly 3 kcal mol^{-1} lower than in the absence of this anion. However, unlike the *i*Pr-substituted system, the thermodynamic driving force for pathway B in the *t*Bu-substituted system was found to decrease upon addition of BF_4^-. Thus, at −40 °C this pathway proceeds downhill with a small driving force of 1.8 kcal mol^{-1}, while at 25 °C it actually constitutes an uphill process, with a free-energy increase of 1.0 kcal mol^{-1}. Nonetheless, even though these energy differences are not as pronounced as in the *i*Pr-substituted system, they are still qualitatively consistent with the experimental findings. As for the unobserved intermediates **11** and **12**, the inclusion of BF_4^-, while maintaining **12** as the more stable species (albeit to a lesser extent than in the absence of the anion), leads to a significant increase in the energy gap between **12** and both complexes **7** and **8**. This renders **12** a transient species on the reaction profile, rather than a stable intermediate (as found in the absence of BF_4^-), and this supports the involvement of this intermediate in the reaction mechanism while accounting for the fact that it was not observed experimentally.

In summary, the inclusion of BF_4^- in the proposed reaction pathways was found to significantly improve the agreement between the computed energies of the various complexes and the experimental results. Moreover, the overall effect of BF_4^- on the reaction profiles was to increase the preference for pathway B, thereby reinforcing our previous conclusion that C–H oxidative addition in the PCP–rhodium systems is directly promoted by CO.

Effect of pincer ligand composition on the reaction with CO–phosphinite versus phosphine: As discussed above, altering the alkyl substituents on the PCP donor groups from isopropyl to the bulkier *tert*-butyl leads to changes in the stabilities of the aryl–hydrido complexes relative to the agostic complexes, but does not change the basic reactivity patterns observed for the two systems. In order to further explore the effect of pincer ligand composition on the behavior of these systems, we chose to replace the PCP-type ligand **5** with a phosphinite-based one, namely, POCOP-type ligand **13** (Scheme 3). This ligand is very similar in structure to ligand **5**, albeit having oxygen atoms instead of methylene moieties in the ligand "arms."

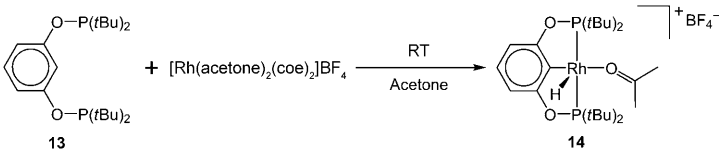

13 14

Scheme 3. Preparation of POCOP–Rh^{III} complex **14**.

Ligand **13** (and derivatives thereof) has been employed by Brookhart and co-workers for the preparation of iridium complexes, which were mainly applied as dehydrogenation catalysts.[25] These POCOP complexes were found to outperform their PCP analogues, which were based on ligand **5**, in catalyzing the cyclooctane/*tert*-butylethylene transfer dehydrogenation reaction. The higher activity of the POCOP complexes was attributed to the electron deficiency of the phosphinite-based ligands relative to the phosphine-based PCP ligand.[25c] It was suggested, for example, that the catalytically active PCP–Ir^I system is inhibited due to oxidative addition of *tert*-butylethylene to the electron-rich metal center, which leads to a catalytic dead-end in the form of a stable Ir^{III}–hydrido–vinyl product. The POCOP–Ir^I system, on the other hand, is suggested to be more electron-deficient and therefore only capable of olefin coordination, without oxidative addition, thereby preventing the catalyst from being inhibited.

The notion that ligand **13** is more electron-poor than **5**, which was the underlying tenet in the work of Brookhart and co-workers, was also the initial assumption in our work. Thus, we set to explore the reactivity of cationic rhodium complex **14** (Scheme 3) towards CO, with the expectation that it would reflect the electron-deficient character of the pincer ligand and would be more prone to reductive elimination than **6**. Complex **14** was prepared in a manner completely analogous to complexes **2** and **6**, by reacting ligand **13** with one equivalent of $[Rh(acetone)_2(coe)_2]BF_4$ in acetone, at room temperature. This led to facile C–H cleavage, as observed for the PCP systems, with formation of complex **14** in high yield. The $^{31}P\{^1H\}$ NMR spectrum of this complex

in $CDCl_3$ exhibits a doublet at $\delta = 189.42$ ppm ($^1J(Rh,P) = 122.4$ Hz), and its ^1H NMR spectrum features a hydride signal at $\delta = -26.87$ ppm (doublet-of-triplets, $^1J(Rh,H) = 53.8$ Hz, $^2J(P,H) = 9.7$ Hz), which is typical of a hydride ligand *trans* to a vacant coordination site, as also observed for complexes **2** and **6**. Full characterization of complex **14** (see the Experimental Section), including X-ray crystallography (see below), revealed a structure that is completely analogous to that of complex **6**.

Crystals of **14** suitable for X-ray diffraction were grown at room temperature from a solution of **14** in acetone overlaid with diethyl ether (see Table 1 for the crystallographic parameters). Complex **14** was found to crystallize in the $P2_1/c$ space group, with each asymmetric unit comprised of two complex cations of nearly identical structure, as well as two noncoordinated BF_4^- counterions. The molecular structure of complex **14**, which is presented in Figure 4, is analogous

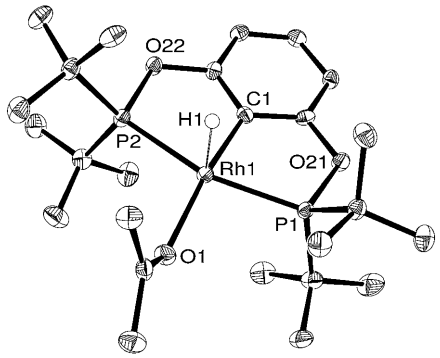

Figure 4. ORTEP drawing of complex **14** (50% probability level). Only one of the two molecules in the asymmetric unit is shown. Hydrogen atoms (except for hydride) and the BF_4^- counterion have been omitted for clarity.

to that of complex **6**, with a square-pyramidal coordination arrangement, including an axial hydride ligand *trans* to an empty coordination site,[26] as well as an equatorial acetone ligand *trans* to the aryl moiety. Selected bond lengths and angles for complex **14** are presented in Table 5.

As in the case of complex **6**, the BF_4^- counterion of **14** is outer-sphere in the crystal structure, but in solution it is fluxionally coordinated to the metal center. This is clearly indicated by the $^{19}F\{^1H\}$ NMR spectrum of **14** in $CDCl_3$, which exhibits an extremely broad BF_4^- signal at $\delta = -165.4$ ppm ($\Delta\nu_{1/2} \approx 1100$ Hz). However, in contrast to complex **6**, the ^1H NMR spectra of **14** in [D_6]acetone and $CDCl_3$ exhibit very similar chemical shifts for the hydride ligand ($\delta = -26.18$ vs. -26.87 ppm, respectively), and this indicates that complex **14** has similar coordination environments in the two solvents. Nonetheless, the above observations suggest that the overall steric effects exerted by POCOP ligand **13** are very similar to those of PCP ligand **5**, as might have been expected from the fact that they both bear *tert*-butyl substituents.

Table 5. Selected bond lengths [Å] and angles [°] for complex **14**.[a]

Rh1–C1	1.989(3)	Rh1–P1	2.3074(7)
Rh1–O1	2.1478(18)	Rh1–P2	2.3303(7)
C1-Rh1-P1	80.36(8)	O1-Rh1-P2	104.30(5)
C1-Rh1-P2	80.29(8)	C1-Rh1-O1	171.11(9)
O1-Rh1-P1	94.61(5)	P1-Rh1-P2	160.55(3)

[a] The asymmetric unit in the crystal of complex **14** contains two nearly identical complexes. This table contains the crystal data for one of these complexes.

The close structural similarity between complexes **6** and **14**, coupled with the assumption that the phosphinite ligand renders complex **14** more electron-deficient than complex **6**, led us to expect similar reactivity under CO, with complex **14** being somewhat more prone to C–H reductive elimination than complex **6**. In other words, we expected complex **14** to yield an agostic product upon reaction with CO, with this reaction being even more facile than in the case of complex **6**. However, when complex **14** was treated with CO a very different result was observed. Addition of one equivalent of CO to a solution of **14** in $CDCl_3$ afforded a new complex, which gave rise to a sharp doublet in the $^{31}P\{^1H\}$ NMR spectrum, at $\delta = 203.76$ ppm ($^1J(Rh,P) = 105.8$ Hz). More intriguingly, however, the ^1H NMR spectrum of the new complex exhibited a distinct hydride signal at $\delta = -12.88$ ppm (doublet, $^1J(Rh,H) = 41.1$ Hz), which clearly indicated that this complex is not an agostic species, contrary to our initial expectations. Furthermore, the new complex was found to decompose at room temperature, in clear contrast to agostic complexes **3** and **7**, both of which were found to be thermally robust. In fact, the new complex could only be isolated in relatively pure form when prepared in situ at low temperature (e.g., −20 °C), and so its full characterization was also accomplished at low temperature (−40 °C).

The $^{31}P\{^1H\}$ NMR spectrum of the new complex at −40 °C featured a doublet at $\delta = 203.59$ ppm ($^1J(Rh,P) = 105.7$ Hz), and its hydride ligand gave rise to a doublet at $\delta = -12.36$ ppm ($^1J(Rh,H) = 40.8$ Hz) in the ^1H NMR spectrum. The $^{13}C\{^1H\}$ NMR spectrum of this complex was found to contain a single carbonyl signal at $\delta = 188.50$ ppm (doublet-of-triplets, $^1J(Rh,C) = 63.5$ Hz, $^2J(P,C) = 9.1$ Hz), which indicates the presence of a single terminal carbonyl ligand. Indeed, when ^{13}C-labeled CO was used to prepare this new complex, its $^{31}P\{^1H\}$ NMR signal exhibited an additional doublet splitting ($^2J(C,P) = 8.5$ Hz),[27] which confirms the existence of a single CO ligand. Moreover, neither the hydride nor the carbonyl NMR signals of the labeled complex exhibited any observable $^1H,^{13}C$ coupling, which strongly indicated that these two ligands are in a *cis* configuration.[13] These NMR data, together with the overall similarity between the NMR spectra of the new complex and its precursor complex, **14**, led us to conclude that the new complex was **15** (see Scheme 4), an aryl–hydrido–monocarbonyl Rh^{III} species. It should be noted that this complex is reminiscent of the unobserved intermediates **9** and **11** mentioned above (Scheme 2).

As can be seen in Scheme 4, complex **15** is portrayed as a square-pyramidal structure, in a manner similar to complex

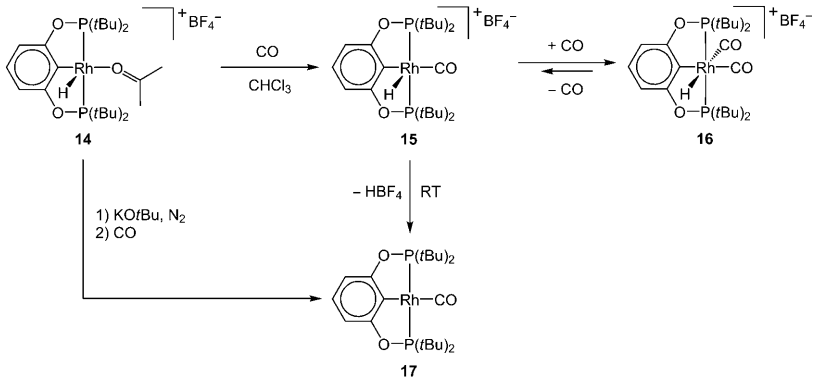

Scheme 4. Reactions of the POCOP–Rh complexes with CO.

14. However, as in the case of **14**, this representation simply serves to emphasize that the coordination site *trans* to the hydride ligand is occupied by highly labile ligands. Thus, like complex **14**, complex **15** was found to bind the BF_4^- counterion, as indicated by its relatively broad ^{19}F NMR signal at $\delta = -152.48$ ppm ($\Delta\nu_{1/2} = 60$ Hz). Moreover, the ^1H NMR spectrum of **15** indicates that it also binds the residual acetone molecules released into the solution when **14** reacts with CO, as indicated by a broadening of the acetone signal ($\Delta\nu_{1/2} \approx 13$ Hz, as compared with 1–2 Hz for free acetone). The binding of acetone, which competes with the coordination of BF_4^- (see Scheme 5), appears to be responsible for concentration-dependent changes in the chemical shift observed for the hydride signal of complex **15**.[28]

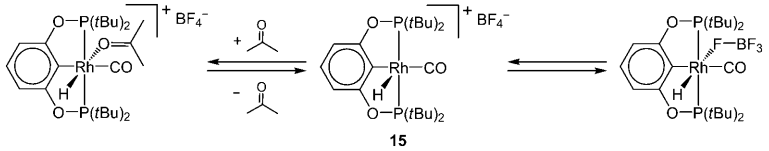

Scheme 5. Reversible binding of the BF_4^- counterion and acetone to complex **15**.

Addition of a second equivalent of CO to complex **15** yielded yet another new complex, **16**, as shown in Scheme 4. This complex, which is analogous to complexes **4** and **8**, gave rise to sharp NMR signals at room temperature, in marked contrast to its PCP-type analogues, which under the same conditions were either unobserved (**8**) or gave rise to extremely broad NMR signals (**4**). The room-temperature $^{31}P\{^1H\}$ NMR spectrum of **16** in $CDCl_3$ exhibited a sharp doublet at $\delta = 210.52$ ppm ($^1J(Rh,P) = 93.6$ Hz), and its ^1H NMR spectrum featured a sharp hydride signal at $\delta = -9.53$ ppm (multiplet). The $^{13}C\{^1H\}$ NMR spectrum of this new complex (recorded at $-40\,^\circ C$ to prevent decomposition[29]) was found to contain two carbonyl signals at $\delta = 184.55$ ppm (multiplet, $^1J(Rh,C) = 37.4$ Hz) and $\delta = 182.19$ ppm (doublet-of-triplets, $^1J(Rh,C) = 45.7$ Hz, $^2J(P,C) = 6.7$ Hz), thus indicating the presence of two carbonyl ligands. This was corroborated by examining the $^{31}P\{^1H\}$ NMR signal of the ^{13}CO-labeled complex, which featured an additional triplet splitting ($^2J(C,P) = 6.7$ Hz), which is consistent with the presence of two CO ligands. This labeled complex also confirmed the relative positions of the hydride and carbonyl ligands in **16**, as was also described above for complex **8**. Thus, the NMR signals for the hydride ligand and one of the carbonyl ligands ($\delta(^{13}C) = 184.55$ ppm) featured a large $^1H,^{13}C$ coupling constant of 62.3 Hz, thereby indicating a *trans* configuration for these two ligands, whereas the second CO ligand featured no observable $^1H,^{13}C$ coupling, which is consistent with a *cis* configuration relative to the hydride.[13]

Complex **16** proved to be stable enough at mildly low temperatures (e.g., $-20\,^\circ C$), even in the absence of excess CO, to allow for the isolation of its crystals. Thus, crystals of **16** suitable for X-ray diffraction were grown at $-20\,^\circ C$ from a solution of **16** in dichloromethane overlaid with pentane (see Table 1 for the crystallographic parameters). This complex was found to crystallize in the *C*2/*c* space group, with each asymmetric unit containing one cationic complex, two noncoordinated BF_4^- counterions, and one dichloromethane molecule. The existence of two BF_4^- counterions per complex instead of just one (as would be expected for a monocationic complex) is due to the presence of HBF_4 as a contaminant in the crystal. This HBF_4 is formed as a consequence of the thermal decomposition of **16**, as will be discussed below.

The molecular structure of complex **16**, which is shown in Figure 5, is consistent with the conclusions drawn from its NMR spectra. Thus, the complex features an octahedral coordination geometry, with two CO ligands in a *cis* configuration. The axial hydride ligand was not located in the elec-

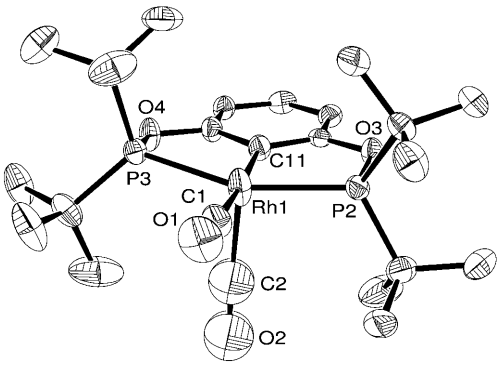

Figure 5. ORTEP drawing of complex **16** (50% probability level). Hydrogen atoms, two BF_4^- counterions,[33] and a solvent molecule have been omitted for clarity.

tron-density map. As can be seen in Figure 5, the axial CO ligand of **16** exhibits considerable disorder in the crystal structure, which is probably due to partial loss of this ligand in the solid state. This disorder precludes accurate measurement of the bond lengths associated with this CO ligand. The second CO ligand, which does not experience significant disorder, has a C–O bond that measures 1.126(7) Å, which is significantly shorter than the average value for terminal CO ligands in known rhodium carbonyl complexes ((1.139 ± 0.024) Å),[30] and is actually comparable in length to free CO (1.128 Å[31]). Furthermore, the Rh–C bond for this ligand measures 1.956(6) Å, which is significantly longer than the average value for terminal CO ligands in known rhodium carbonyl complexes ((1.858 ± 0.046) Å).[30,32] For other selected bond lengths and angles in complex **16** see Table 6.

Table 6. Selected bond lengths [Å] and angles [°] for complex **16**.

Rh1–C11	2.034(5)	Rh1–P3	2.3335(14)
Rh1–C1	1.956(6)	C1–O1	1.126(7)
Rh1–C2	2.088(11)	C2–O2	1.246(11)[a]
Rh1–P2	2.3309(14)		
C11-Rh1-P2	79.34(15)	P2-Rh1-P3	156.16(5)
C11-Rh1-P3	79.00(14)	C11-Rh1-C2	92.6(3)
C1-Rh1-P2	101.48(17)	C1-Rh1-C2	92.8(3)
C1-Rh1-P3	99.14(17)	Rh1-C1-O1	176.6(6)
C11-Rh1-C1	174.4(2)	Rh1-C2-O2	177.8(9)

[a] The axial CO ligand in complex **16** exhibits significant disorder (due to partial decomposition), and therefore the C–O bond length measured for this ligand is expected to be highly inaccurate (regardless of the computed error).

The partial loss of the axial CO ligand, which was manifested in the crystal of complex **16**, was also found to occur in solution. Thus, when a solution of complex **16** in $CDCl_3$ under excess CO was purged with argon for a few minutes, a small amount of complex **15** was regenerated, thereby indicating that the axial carbonyl ligand is indeed relatively labile. In other words, the reaction of complex **15** with CO to afford **16** is reversible, as was also observed for the PCP-type systems (**3**–**4**, **7**–**8**).

The decarbonylation of **16** accounts for one aspect of the instability of the POCOP-type Rh^{III} carbonyl complexes described herein. Another aspect of this instability is related to its decarbonylation product, complex **15**. It was found that when this complex was directly generated by the reaction of **14** with CO at room temperature, its formation was accompanied by the appearance of another distinct species. This side-product gave rise to a doublet in the $^{31}P\{^1H\}$ NMR spectrum at $\delta = 215.23$ ppm ($^1J(Rh,P) = 156.7$ Hz) and lacked any hydride signal in the ^1H NMR spectrum. The significantly larger $^{103}Rh,^{31}P$ coupling constant observed for this complex, as compared with that of **15** (105.8 Hz), suggested that the new species possesses a more electron-rich rhodium center. Indeed, careful analysis of the new complex revealed it to be the neutral Rh^I complex **17** (Scheme 4). It should be noted that, as part of the identification process, complex **17** was also prepared through an alternative route, by treating complex **14** with a base (e.g., KO*t*Bu) under an atmosphere of dinitrogen, followed by reaction with CO gas, as shown in Scheme 4.

Crystals of **17** suitable for X-ray diffraction were grown at −35 °C from a solution of **17** in chloroform overlaid with pentane (see Table 1 for the crystallographic parameters). Complex **17**, which crystallized in the $P\bar{1}$ space group, is shown in Figure 6. As would be expected of a tetracoordinate Rh^I complex, **17** features a distorted, yet virtually flat square-planar coordination geometry. The CO ligand of this complex has a rather short C–O bond (C1–O3 = 1.133(4) Å), which is quite close in length to free CO. However, in contrast to complex **16**, the Rh–C bond length associated with the CO ligand in **17** is rather close to the average value found for rhodium carbonyl complexes (see above), with Rh1–C1 = 1.887(3) Å. Other selected bond lengths and angles for complex **17** are given in Table 7.

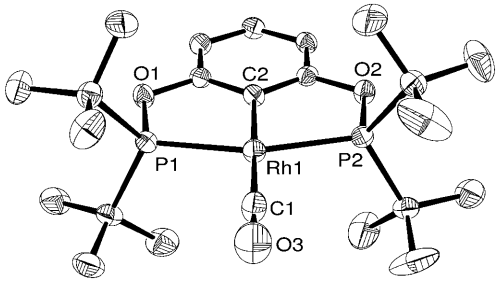

Figure 6. ORTEP drawing of complex **17** (50 % probability level). Hydrogen atoms have been omitted for clarity.

Table 7. Selected bond lengths [Å] and angles [°] for complex **17**.

Rh1–C2	2.043(3)	Rh1–P2	2.2829(11)
Rh1–C1	1.887(3)	C1–O3	1.133(4)
Rh1–P1	2.2816(9)		
C2-Rh1-P1	78.66(8)	C2-Rh1-C1	178.75(11)
C2-Rh1-P2	78.70(8)	P1-Rh1-P2	157.32(3)
C1-Rh1-P1	101.02(9)	Rh1-C1-O3	178.9(3)
C1-Rh1-P2	101.64(9)		

The formation of neutral complex **17** from cationic complex **15** necessarily involves the elimination of HBF_4, which appears in the ^1H NMR spectrum as a broad singlet at $\delta =$ 9–10 ppm (in $CDCl_3$). This accounts for the presence of HBF_4 in the crystal of complex **16**, as mentioned above. The direct source of this acid was initially believed to be complex **15**, but subsequent DFT calculations suggested that a more likely source is an unobserved agostic species derived from **15** (see below). It should also be noted that the liberation of HBF_4 was found to be a reversible process, since treatment of a solution of pure complex **17** in chloroform with a 5-fold excess of HBF_4 (etherate complex) resulted in the formation of complex **15**. However, even in the presence of excess HBF_4 the reaction was not complete, with only about 60 % conversion (**15**/**17** ≈ 1.5:1; based on ^{13}P NMR signal integration).

DFT examination of the phosphinite-based pincer system: The marked differences in reactivity between the phosphine- and phosphinite-based pincer systems prompted us to study the phosphinite system in greater detail using DFT calculations. Our computational examination encompassed the experimentally observed aryl–hydrido complexes **15** and **16**, as well as the unobserved agostic species **18** and **19** (see Scheme 6). All structures were initially optimized with the exclusion of the BF_4^- counterion, which was subsequently added to account for the experimentally observed involvement of this counterion in the POCOP system, especially vis-à-vis complex **15**. As in the case of the PCP–rhodium complexes, the BF_4^- counterion was appended to the POCOP–rhodium species either as an inner-sphere ligand (in complexes **15** and **18**, where this is sterically feasible), or in direct interaction with the hydride ligand or agostic proton (in all complexes).

Selected geometric parameters for the computed cationic POCOP complexes are presented in Table 8. It should be noted that complex **16**, for which crystallographic data are available, exhibits good agreement between the optimized and experimental geometries, and this further substantiates the general accuracy of the optimized geometries. Examination of the optimized geometric data for all four POCOP complexes reveals general similarities to the PCP systems, especially concerning the carbonyl ligands. Thus, the Rh^{III} aryl–hydrido POCOP complexes have longer Rh–CO bonds and shorter C–O bonds than the agostic Rh^{I} complexes; the CO ligands in the dicarbonyl complexes have different Rh–CO and C–O bond lengths, depending on their position relative to the aryl moiety; and the trigonal-bipyramidal dicarbonyl complex (**19**) exhibits markedly bent CO ligands. However, closer examination of the geometric data reveals a few important differences between the POCOP and PCP systems, especially regarding complexes **18** and **19**. Firstly, these agostic complexes possess shorter Rh–C_{ipso} and Rh–H bonds, and longer C_{ipso}–H bonds, than their PCP counterparts, and this indicates a higher degree of C–H bond activation in the POCOP complexes. This may well be related to the observed acidity of the POCOP system, as will be further elaborated below. Secondly, complexes **18** and **19** exhibit longer Rh–CO bonds than their PCP analogues, which indicates weaker interactions between Rh and CO in the POCOP system. It should be noted, however, that the carbonyl C–O bonds in the POCOP system are of comparable length to the PCP systems, thereby implying that Rh→CO π back-donation is not significantly affected by the change in pincer ligand.

Table 8. Selected optimized interatomic distances [Å], angles [°], and total natural charges (Q) on CO ligands for the POCOP–rhodium–carbonyl complexes shown in Scheme 6.[a]

Optimized data	**15**	**16**	**18**	**19**
Rh–P1	2.337	2.377	2.327	2.384
Rh–P2	2.337	2.371	2.327	2.385
Rh–C_{ipso}	2.016	2.058	2.127	2.283
C_{ipso}–H	2.410	2.468	1.150	1.126
Rh–H	1.497	1.555	1.861	2.010
Rh–C (CO_{trans})	1.934	1.940	1.861	1.884
Rh–C (CO_{cis})	–	1.996	–	1.933
C–O (CO_{trans})	1.141	1.139	1.148	1.149
C–O (CO_{cis})	–	1.136	–	1.147
∢OC_{trans}-Rh-C_{ipso}	175.7	172.9	175.2	137.6
∢Rh-C_{trans}-O	175.6	177.1	177.9	172.4
∢OC_{cis}-Rh-C_{ipso}	–	88.4	–	106.0
∢Rh-C_{cis}-O	–	177.0	–	165.8
∢Rh-C_{ipso}-C_{para}	178.9	178.1	155.8	142.2
Q(CO_{trans})	0.266	0.302	0.225	0.246
Q(CO_{cis})	–	0.222	–	0.238

[a] CO_{trans} and CO_{cis} refer to the CO ligands positioned *trans* and *cis* to the C_{ipso} atom, respectively.

The computed energies of the POCOP complexes, in the absence and presence of BF_4^-, are presented in Figure 7. As can be seen in this figure, the inclusion of BF_4^- alters the stabilities of the various POCOP species, as was previously found for the PCP systems. In the majority of cases the interaction with BF_4^- is a stabilizing one, although the extent of stabilization varies considerably with temperature and among the different species. Particularly notable is the stabilization of complex **15** by a metal-bound BF_4^-, which amounts to 4.4 kcal mol^{-1} at room temperature and 7.6 kcal mol^{-1} at −40 °C. This strong interaction is consistent with the experimentally observed broadening of the BF_4^- signal in the ^{19}F NMR spectrum of **15** (see above), which is a telltale sign of counterion coordination. More modest stabilization is exhibited by complexes **18** and **19**, in which the lowest energy is attained by the interaction of BF_4^- with the agostic proton, especially at low temperature. In the case of complex **18**, the opposite effect is also evident, whereby interaction of BF_4^- with the metal center is energetically unfavorable at both temperatures. However, the most pronounced destabilization is exhibited by complex **16**, for which the interaction with BF_4^- is endothermic by 7.2 kcal mol^{-1} at room temperature and 4.7 kcal mol^{-1} at −40 °C. In other words, complex **16** and its counterion are most likely to exist in solution as a separated ion pair, in contrast to the other three complexes.

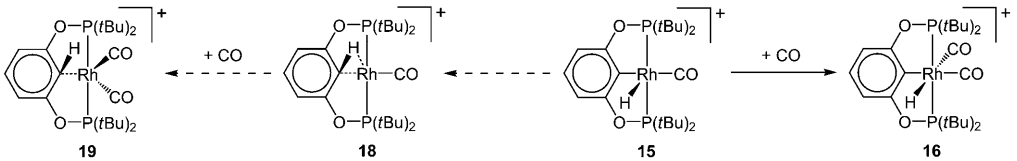

Scheme 6. Reactions of the POCOP pincer system with CO, as examined by DFT analysis.

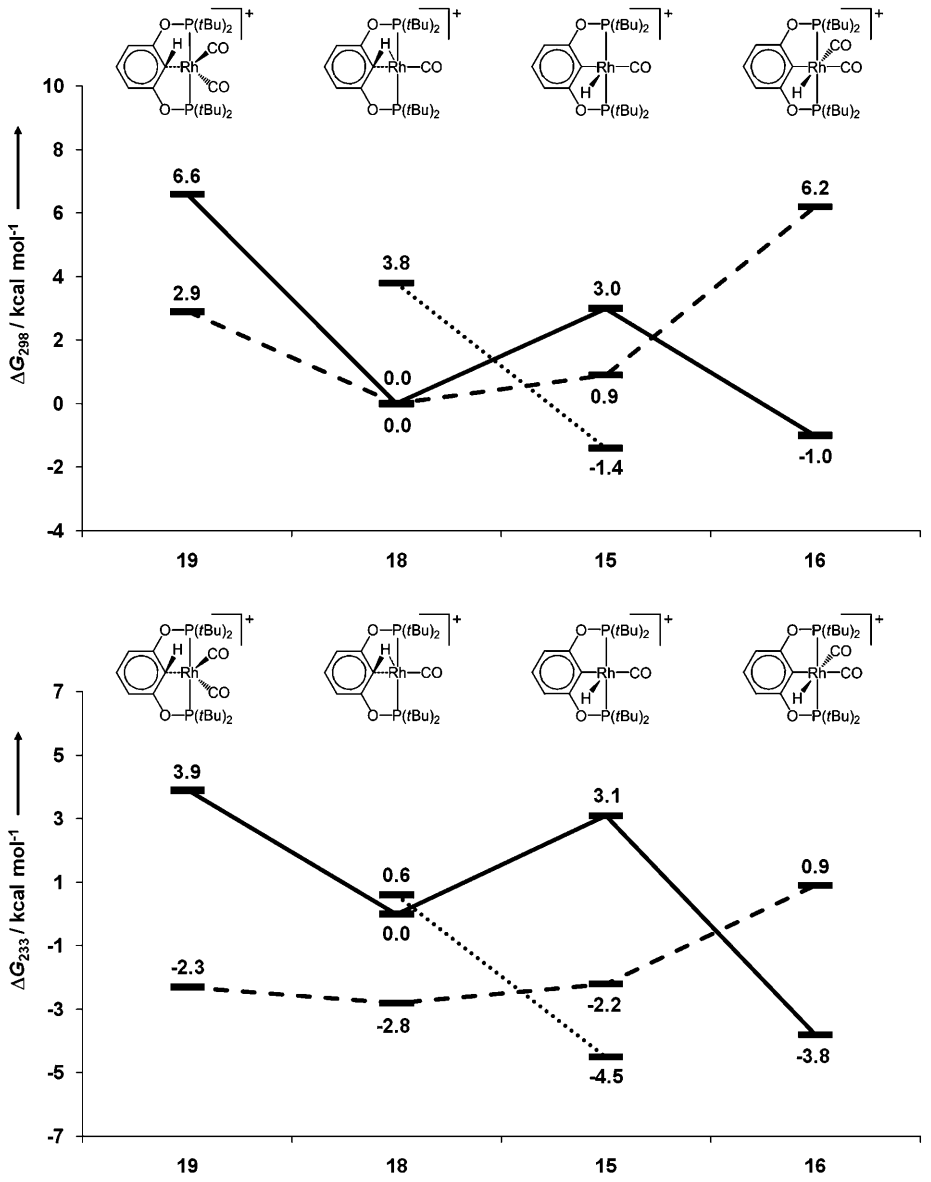

Figure 7. Relative energies of the cationic POCOP complexes (——), as well as their outer sphere (BF_4^H: -----) and inner sphere (BF_4^{Rh}: •••••) adducts with the BF_4^- counterion, at 25 °C (top) and −40 °C (bottom). The monocarbonyl agostic complex with no BF_4^- interaction (**18**) is taken as the reference energy point.

The above results pertaining to the effects of BF_4^- designate complex **15**-BF_4^{Rh} (with a rhodium-bound BF_4^-) as the most stable of the examined species, followed closely by complex **16** (with no direct BF_4^- interactions). The stability of these two species, as indicated by our DFT calculations, is consistent with the fact that both were experimentally isolated. Moreover, the small energy difference between **15**-BF_4^{Rh} and **16** accounts for their experimentally observed interconversion, but it should be borne in mind that such interconversion must proceed through the high-energy "naked" complex **15**, which possesses an empty coordination site. Further insight into the observed behavior of the POCOP system is gained when complexes **18** and **19** are considered. Interestingly, the unobserved complex **18**-BF_4^H (with BF_4^- bound to the agostic proton) is calculated to be only about 1.5 kcal mol^{-1} uphill from **15**-BF_4^{Rh}, which renders it highly accessible from this observed species. Moreover, as was already suggested by the elongation of the C_{ipso}–H bond in complex **18**, analysis of the electron density distribution indicates that the agostic proton in this complex is highly acidic—certainly more than the hydride ligand in **15**. This enhanced acidity can account for the observed release of HBF_4 from the POCOP system, especially in light of the strong interaction between BF_4^- and the agostic proton in **18**-BF_4^H. As for complex **19**, its high energy, relative to the other species, is consistent with the fact that it was not observed experimentally.

All in all, the above results highlight the important differences between the POCOP and PCP systems. Although both pincer ligands are capable of stabilizing cationic aryl–hydrido dicarbonyl Rh^{III} species, they diverge in behavior with respect to all other carbonyl complexes. Thus, the POCOP system supports a stable cationic aryl–hydrido monocarbonyl Rh^{III} species, whereas in the PCP system such a complex is highly unstable. Furthermore, the PCP ligands support stable agostic monocarbonyl Rh^I complexes, both as isolable compounds and stable (albeit unobserved) intermediates, whereas in the POCOP system such species are notably unstable. These significant dissimilarities between the two ligand frameworks originate from their different electronic properties, as will be discussed below.

Reaction of agostic complex 3 with the donor ligand acetonitrile—experimental and theoretical examination: The reactions of CO with the agostic PCP systems described above appear to suggest that while the first CO ligand plays its classical role as a dominant π-acceptor, the additional CO molecule does not behave as an acceptor, but rather as a predominantly donor ligand. In order to probe this assertion, we explored the reactivity of agostic complex **3** towards

acetonitrile, which is commonly accepted as a σ-donor with only weak π-acceptor ability.[34] Thus, complex **3** was treated with a small excess (1.7 equiv) of CH_3CN in chloroform, and this was found to afford a new species in virtually quantitative yield (based on the ^{31}P NMR spectrum). At room temperature, this complex gave rise to a broad doublet at $\delta =$ 81.83 ppm ($^1J(Rh,P) \approx 80$ Hz; $\Delta\nu_{1/2} \approx 120$ Hz) in the $^{31}P\{^1H\}$ NMR spectrum, as well as a broad singlet at $\delta =$ −15.89 ppm ($\Delta\nu_{1/2} \approx 100$ Hz) in the ^1H NMR spectrum, due to a hydride ligand. Another broad singlet ($\Delta\nu_{1/2} \approx 85$ Hz) was observed in the ^1H NMR spectrum at $\delta = 2.10$ ppm, while the rest of the spectrum showed no notable broadening. When the solution was cooled to −30 °C, the broad signals narrowed and became well-resolved, and this allowed full characterization of the new product, which emerged as complex **20**, an analogue of **4** with a CH_3CN molecule instead of the carbonyl ligand *trans* to the hydride (see Scheme 7, top). In fact, the broad room-temperature ^1H NMR signal at $\delta = 2.10$ ppm turned out to be a convoluted combination of signals for the free and bound CH_3CN. The relative configuration of the carbonyl and nitrile ligands in **20** was conclusively determined by analyzing the NMR spectra of a complex containing ^{13}C-labeled CO. The hydride signal in the ^1H NMR spectrum and the carbonyl signal in the ^1H-coupled ^{13}C NMR spectrum of this complex exhibited no observable $^1H,^{13}C$ coupling, which strongly indicates that the two ligands are in the *cis* configuration.[13]

The broad NMR signals observed for complex **20** at room temperature were reminiscent of the observations made for complex **4** under excess CO, as described in our previous report.[7] Moreover, when complex **3** was treated with about half an equivalent of CH_3CN in chloroform, both complexes **3** and **20** were observed in the solution, and their mixture gave rise to broad signals in both the ^1H and $^{31}P\{^1H\}$ NMR spectra. The coexistence of the two species in solution made it possible to employ the SST technique in order to investigate whether the two species were in mutual equilibrium, as was previously done for a mixture of **3** and **4** (in the absence of excess CO).[7] Indeed, when the hydride ligand of **20** (broad singlet at $\delta = -15.89$ ppm) was selectively irradiated at room temperature, significant decrease in the intensity of the ^1H NMR signal corresponding to the agostic proton (broad singlet at $\delta = 4.20$ ppm) was observed, clearly indicating that species **3** and **20** were in dynamic equilibrium. When complex **3** was dissolved in neat acetonitrile, complex **20** was produced in quantitative yield (based on the ^{31}P NMR spectrum) and gave rise to sharp NMR signals. In this case, the large excess of acetonitrile drove the **3**⇄**20** equilibrium completely to the product side, as was also observed for complex **3** under excess CO.[7]

As far as the overall process is concerned, the reaction of complex **3** with CH_3CN bears great resemblance to its reaction with CO. In other words, the two ligands, which are significantly different in their electronic properties, exert a similar effect on agostic complex **3**. In order to account for this similarity, we proposed two mechanistic pathways for the acetonitrile reaction, which are virtually identical to those proposed for CO, as shown in Scheme 7 (bottom). The two pathways were then examined using DFT calculations. Selected geometric parameters and ligand charges for the optimized acetonitrile complexes are listed in Table 9, and the reaction profiles, calculated for 25 and −40 °C, are shown in Figure 8.

The optimized geometries for the acetonitrile-containing complexes display notable differences from those of the analogous carbonyl complexes. Thus, aryl–hydrido complex **20** exhibits shorter Rh−H and Rh−CO bonds, as well as a longer C−O bond, relative to the corresponding bonds in dicarbonyl complexes **4** and **8**, and this indicates the presence of stronger metal–hydride and metal–carbonyl interactions in complex **20**. Interestingly, the CO ligand in complex **20** (as well as in **TS**(**21**–**20**)) is more electron-rich than the *trans* CO ligands in the dicarbonyl complexes, as indicated by their natural bond orbital (NBO) charges (see Tables 3 and 9). This implies that the carbonyl ligand in complex **20** is either a weaker electron donor or stronger electron acceptor, or both, relative to the corresponding carbonyl ligands in complexes **4** and **8**. As for intermediate **21**, it exhibits

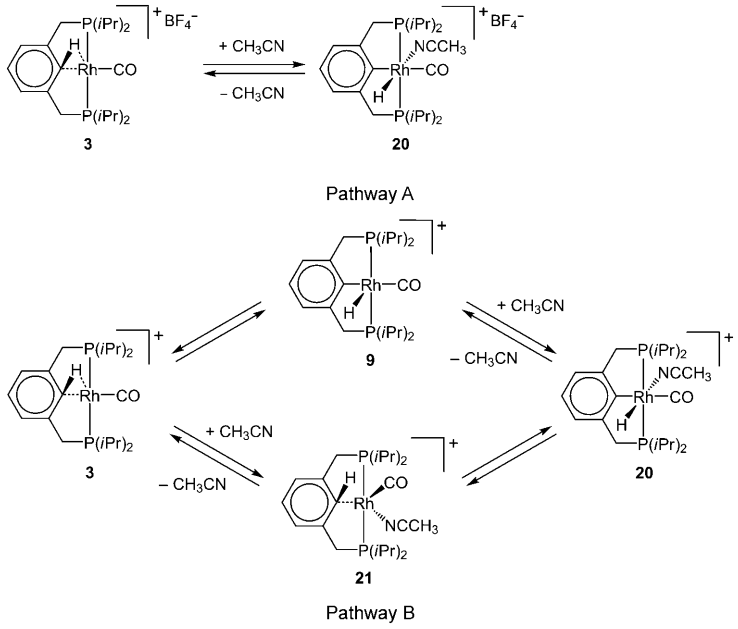

Scheme 7. Top) Reaction of agostic complex **3** with acetonitrile. Bottom) Proposed mechanistic pathways for the reaction of **3** with acetonitrile.

Table 9. Selected optimized interatomic distances [Å], angles [°], and total natural charges (Q) on CO and CH_3CN ligands for the PCP–rhodium–carbonyl–acetonitrile complexes shown in Scheme 7.

Optimized data	**20**	**TS(21–20)**	**21**
Rh–P1	2.344	2.342	2.373
Rh–P2	2.357	2.346	2.388
Rh–C_{ipso}	2.080	2.122	2.696
C_{ipso}–H	2.431	1.426	1.095
Rh–H	1.533	1.604	2.536
Rh–C (CO)	1.928	1.896	1.805
Rh–N (CH_3CN)	2.171	2.320	2.094
C–O (CO)	1.143	1.147	1.155
∢OC-Rh-C_{ipso}	171.7	163.0	126.8
∢Rh-C_{ipso}-C_{para}	179.1	168.6	114.9
Q(CO)	0.136	0.194	0.241
Q(CH_3CN)	0.136	0.094	0.229

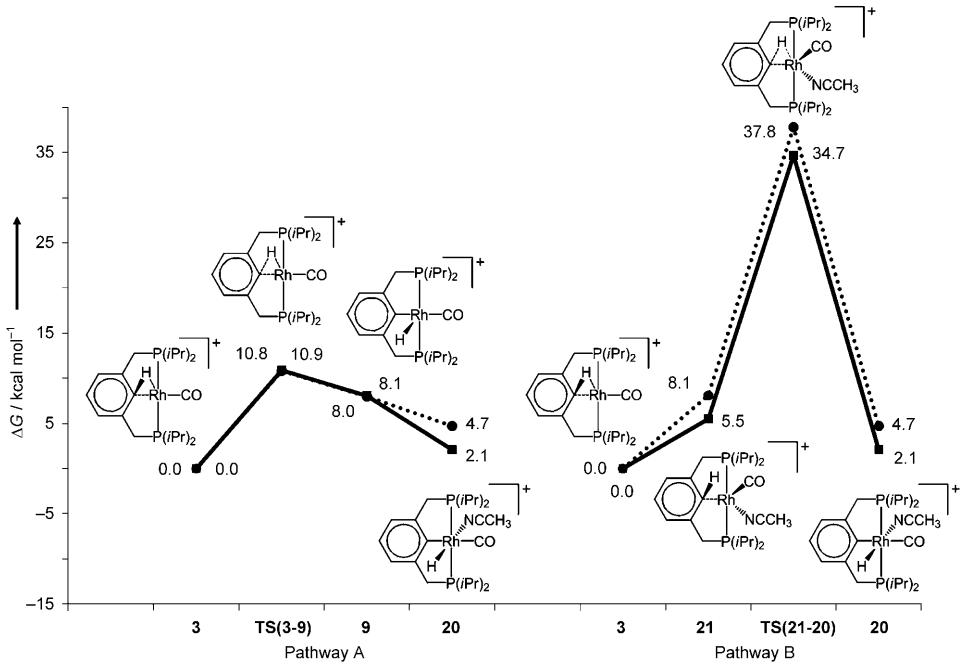

Figure 8. Calculated energy profiles of the proposed reaction pathways for the addition of CH_3CN to agostic complex **3** at 25 °C (···●···) and −40 °C (——■——). The agostic complex **3** is taken as the reference energy point.

longer Rh–C_{ipso} and Rh–H bonds, as well as a shorter C_{ipso}–H bond, relative to its dicarbonyl analogues **10** and **12**, and this indicates much weaker activation of the arene C–H bond in intermediate **21**.

As can be seen in Figure 8, the energy profiles for the reaction of agostic complex **3** with CH_3CN are significantly different, both qualitatively and quantitatively, from those of its reaction with CO (see Figure 2, top).[35] The most prominent feature of these reaction profiles is the extremely high kinetic barrier for pathway B ($\Delta G^{\neq} \approx 35$–$38$ kcal mol^{-1}), as compared with the relatively low kinetic barrier for pathway A ($\Delta G^{\neq} \approx 11$ kcal mol^{-1}). This clearly indicates that the reaction of complex **3** with CH_3CN cannot take place along pathway B, leaving pathway A as the only available option. In other words, the reaction of complex **3** with CH_3CN occurs only by spontaneous C–H cleavage in the agostic complex, with subsequent trapping by an incoming acetonitrile ligand. This constitutes a shift in mechanism from the direct promotion pathway observed for the CO ligand to the trapping pathway observed for CH_3CN. The electronic factors behind this mechanistic shift, as revealed by an analysis of the electronic structure of the carbonyl and acetonitrile complexes, will be discussed below.

Electronic structure analysis and the origin of the dual effect of CO: In order to explore the electronic factors behind the intriguing behavior of CO ligands observed in the present work, we analyzed the electronic structure of the above-mentioned carbonyl complexes in terms of donation, back-donation, and repulsion between the metal atom and ligands. It is now generally accepted that transition-metal-mediated oxidative addition of C–H bonds involves transfer of electron density from the bonding σ C–H orbital to the metal atom, and back-donation into the antibonding σ* C–H orbital. The extent of these charge transfers differs at different stages of the interaction. Thus, charge transfer from σ_{C-H} to the metal center comes into effect at relatively long distances between the metal and C–H bond, thereby leading to the formation of a σ complex, which in the case of intramolecular interactions is commonly termed an agostic complex.[36] At shorter distances—usually in the transition state—back-donation intensifies, thus leading to increased electron density in the vicinity of the C–H bond, which eventually results in its cleavage. The interactions between the metal atom and the formally anionic hydrocarbyl and hydrido ligands, which were obtained as a result of the activation process, determine the overall thermodynamics of the C–H oxidative addition reaction. Hence, the exact chemical nature of the C–H bonds, as well as their steric environment, strongly affects the thermodynamics and kinetics of oxidative addition, as has been previously shown.[1d,37] We shall now present a detailed analysis of the influence exerted by the CO ligands, as well as the aromatic moiety, on the critical electron transitions involved in the experimentally observed oxidative addition of aromatic C–H bonds by the mono- and dicarbonyl PCP and POCOP complexes of rhodium. This examination will address all three stages of this

reaction, namely, the agostic interaction, the transition state, and the aryl–hydrido product. In order to facilitate the discussion, Table 10 presents selected Wiberg bond indexes (WBI) that were calculated for mono- and dicarbonyl complexes in the three reaction stages.

Table 10. Wiberg bond indexes (WBI) for selected bonds in the monocarbonyl, dicarbonyl, and acetonitrile–carbonyl complexes and transition states.[a]

Complex	Ligands	Rh–C_{ipso}	Rh–H	C_{ipso}–H	Rh–C_{trans}	$(C–O)_{trans}$	Rh–C_{cis}	$(C–O)_{cis}$
				agostic complexes				
3	PCP(*i*Pr), CO	0.134	0.054	0.740	0.977	2.078	–	–
7	PCP(*t*Bu), CO	0.135	0.057	0.737	0.975	2.070	–	–
18	POCOP(*t*Bu), CO	0.214	0.078	0.677	0.869	2.096	–	–
10	PCP(*i*Pr), 2CO	0.067	0.008	0.808	0.741	2.051	0.691	2.067
12	PCP(*t*Bu), 2CO	0.063	0.006	0.814	0.840	2.009	0.617	2.076
19	POCOP(*t*Bu), 2CO	0.126	0.034	0.746	0.727	2.041	0.604	2.067
21	PCP(*i*Pr), CO, CH_3CN	0.092	0.021	0.872	1.231	2.069	0.477[b]	–
				transition states				
TS(3–9)	PCP(*i*Pr), CO	0.546	0.516	0.223	0.880	2.150	–	–
TS(7–11)	PCP(*t*Bu), CO	0.533	0.495	0.244	0.881	2.141	–	–
TS(18–12)	POCOP(*t*Bu), CO	0.532	0.475	0.255	0.910	2.112	–	–
TS(10–4)	PCP(*i*Pr), 2CO	0.530	0.360	0.356	0.969	2.121	0.878	2.158
TS(12–8)	PCP(*t*Bu), 2CO	0.533	0.350	0.366	0.992	2.102	0.870	2.155
TS(15–19)	POCOP(*t*Bu), 2CO	0.521	0.367	0.341	1.003	2.080	0.876	2.128
TS(21–20)	PCP(*i*Pr), CO, CH_3CN	0.299	0.293	0.435	0.741	2.097	0.123[b]	–
				aryl–hydrido complexes				
9	PCP(*i*Pr), CO	0.410	0.707	0.062	0.662	2.148	–	–
11	PCP(*t*Bu), CO	0.399	0.696	0.062	0.672	2.138	–	–
15	POCOP(*t*Bu), CO	0.402	0.697	0.065	0.666	2.138	–	–
4	PCP(*i*Pr), 2CO	0.387	0.435	0.058	0.639	2.133	0.453	2.166
8	PCP(*t*Bu), 2CO	0.387	0.430	0.058	0.643	2.130	0.458	2.160
16	POCOP(*t*Bu), 2CO	0.383	0.433	0.048	0.646	2.131	0.446	2.165
20	PCP(*i*Pr), CO, CH_3CN	0.443	0.589	0.072	0.643	2.163	0.192[b]	–

[a] Rh–C_{trans} and Rh–C_{cis} refer to the bonds between Rh and the CO ligands positioned *trans* and *cis* to the C_{ipso} atom, respectively. $(C–O)_{trans}$ and $(C–O)_{cis}$ refer to the C–O bonds in these carbonyl ligands. [b] These values refer to the Rh–N bond between rhodium and the acetonitrile ligand.

Agostic complexes: It has previously been shown that the C–H···metal interaction in agostic complexes is highly sensitive to the chemical nature of the C–H bond.[38] In general, this type of interaction is brought about by partial transfer of electron density from the C–H bond to an empty d orbital of a coordinatively unsaturated transition metal, thereby resulting in a three-center, two-electron bond. Electronic and steric effects dictate whether the main contribution to this bonding comes from carbon or hydrogen.[39] The limiting case, whereby bonding occurs predominantly through the hydrogen atom, with negligible contribution from carbon, is known as anagostic bonding, and is typical for sp^3 C–H bonds. In these cases, the energetic preference for η^1-H anagostic bonding over the η^2-C,H agostic interaction usually results from the steric inaccessibility and coordinative saturation of carbon atoms in the alkyl moieties.[40] Formation of agostic complexes of aromatic C–H bonds, on the other hand, is governed by electron donation from the aromatic π orbital into the Rh d_{z^2} orbital, through the *ipso* carbon atom (Scheme 8, left). This interaction dominates over the $\sigma_{C–H}\rightarrow$Rh donation, since the aromatic π orbital is more diffuse and has higher energy than the bonding $\sigma_{C–H}$ orbital.[41]

The $C_{ipso}\rightarrow$Rh electron donation, which involves the p_π orbital on the *ipso* carbon, distorts the aromatic π system, and in order to counteract this unfavorable effect the aromatic ring bends away from the metal center.[42] This bending reduces the participation of the π system in bonding with the metal center and gives rise to interactions between the carbon p_σ orbital and the electron-withdrawing Rh d_{z^2} orbital (Scheme 8, right). Consequently, the $\sigma_{C–H}$ orbital becomes involved in electron donation to the metal center, and this results in the weakening of the C–H bond.[43] In fact, the involvement of the arene π orbitals in the metal–aryl interaction induces a polarization of the $\sigma_{C–H}$ orbital towards the C_{ipso} atom, thereby increasing the acidity of the hydrogen atom and eventually leading to electrophilic C–H bond activation. This is in contrast to the nucleophilic activation typical of η^2-C,H agostic complexes involving aliphatic moieties.

As for the observed differences between the PCP and POCOP systems, these can be traced to the higher electron density on the *ipso* carbon atom of the phosphinite ligand relative to that of the phosphine ligand. This enhanced electron density results in a stronger Rh–C_{ipso} interaction in the mono- and dicarbonyl POCOP agostic complexes (**18** and **19**) relative to their PCP analogues (**7** and **12**). The calculated geometries of the POCOP complexes are consistent with a dominant partial contribution of the carbon p_σ orbital to the overall $C_{ipso}\rightarrow$Rh electron donation. In particular, the angles between the Rh atom and aromatic ring ($\measuredangle$Rh-C_{ipso}-C_{para}) in these complexes are much larger (155.8° for **18** and 142.2° for **19)** than in their PCP analogues (140.3° for **7** and 113.7° for **12**). As a consequence, the POCOP system experiences more pronounced C–H bond activation (see Table 10), accompanied by the accumulation of a higher positive charge on the hydrogen atom (+0.42 in **18** and

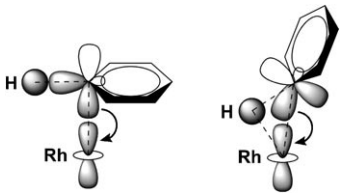

Scheme 8. Key orbital interactions responsible for the Rh···C–H interactions in the agostic complexes.

+0.37 in **19**). The exceptionally large positive charge on the hydrogen atom in complex **18**, as well as its relatively weak C–H bond, sets it as the most probable species responsible for the experimentally observed deprotonation of the monocarbonyl aryl–hydrido POCOP complex **15**. Indeed, the energy data presented above (Figure 7) indicate that complex **18** should be readily accessible, since it is only about 1.5 kcal mol^{-1} higher in energy than the BF_4-stabilized complex **15**. From the mechanistic perspective, complex **18** could be easily formed by dissociation of BF_4^- from complex **15**, with an energy cost of only 4.4 kcal mol^{-1} at room temperature, followed by a thermodynamically favorable C–H reductive elimination, with a calculated activation barrier of only 3.6 kcal mol^{-1}.[44] In the PCP agostic complexes, on the other hand, the C–H-to-metal charge transfer and consequent C–H bond activation are much less significant, and this renders the deprotonation reaction significantly endothermic ($\Delta G_{298} \geq 16.8$ kcal mol^{-1}).

Transition states preceding C–H cleavage: Our calculations show that in both the PCP and POCOP systems the transition states leading from the agostic complex to the C–H oxidative addition product involve a bidirectional electron transfer, whereby donation from the occupied C–H σ orbital to the empty Rh d_{z^2} orbital, and back-donation from the occupied Rh d_{xz} orbital to the empty C–H σ* orbital, are of equal importance (Scheme 9). Both C–H→Rh donation and

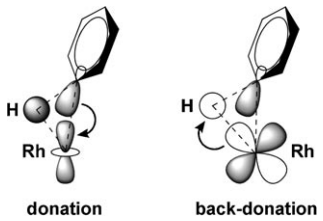

Scheme 9. Key orbital interactions involved in the transition states to C–H bond dissociation.

Rh→C–H back-donation are strongly affected by the presence of CO ligands, which function as both σ-donors and π-acceptors. The relative strength of these interactions is dependent on the energy levels of the transition-metal d orbitals. In the present case, the positive charge on the complex results in the lowering of the rhodium d orbital energies relative to the molecular orbitals of CO, thereby decreasing the back-donating ability of the metal and enhancing σ donation from CO. Indeed, as can be seen from the data presented in Tables 3, 8, and 9, the carbonyl ligands are positively charged in all of the studied complexes, thus implying dominant CO→Rh electron donation and relatively weak Rh→CO back-donation. It is noteworthy that in all of the computed transition states the positive charge on the CO ligands was found to be higher than in the respective reactant and product complexes.

In the square-pyramidal dicarbonyl pincer complexes, the σ(CO)→d_{z^2}(Rh) donation, particularly from the CO ligand *trans* to the aryl moiety (CO_{trans}), competes with the σ(C–H)→d_{z^2}(Rh) donation (see Scheme 10a), and since CO is a much stronger donor than C–H, the latter interaction is im-

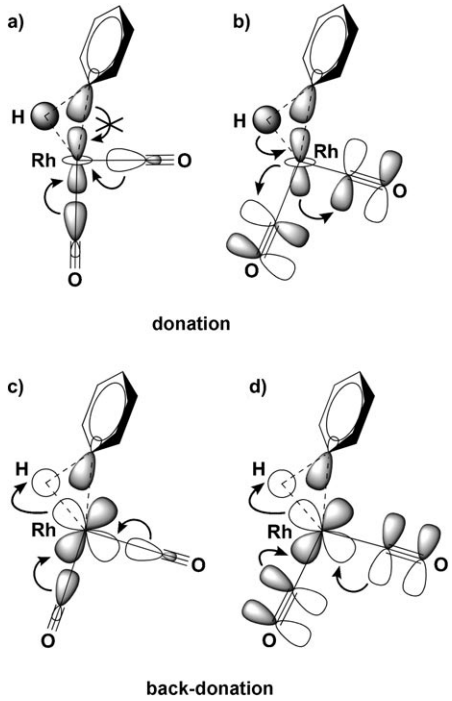

Scheme 10. Influence of CO ligands on C–H→Rh donation (a,b) and Rh→C-H back-donation (c,d) in the transition states leading to C–H bond cleavage.

peded. The system counteracts this unfavorable push–push interaction by bending both CO ligands away from their idealized positions. Thus, CO_{trans} is bent significantly away from the P-Rh-C_{ipso} plane, with the C_{ipso}-Rh-CO_{trans} angle decreasing to 155–163° (Tables 3, 8, and 9), whereas CO_{cis} is bent to a lesser extent, with the C_{ipso}-Rh-CO_{cis} angle increasing by about 10° from the ideal *cis* orientation. Overall, the bending of the CO ligands exerts a very important, multifaceted effect on the interactions between rhodium and the C–H bond in the transition state. Firstly, the C–H→Rh σ donation is significantly facilitated, not only because CO bending reduces the unfavorable CO→Rh σ donation, but also because it allows for some overlap between Rh d_{z^2} and an empty CO π* orbital (Scheme 10b), which renders d_{z^2} even more electrophilic. Secondly, the Rh→C–H σ* back-donation is also assisted by CO bending, since the occupied Rh d_{xz} orbital becomes a stronger electron donor, following its decreased overlap with the CO π* orbital and concomitant decrease in Rh→CO back-donation. In addition, the d_{xz} orbital is rendered more electron-rich by σ donation from both CO ligands, as a consequence of the deviation of the complex geometry from a perfect square pyramid (Scheme 10c). Moreover, symmetry decomposition analysis of the atomic CO orbitals indicates that the filled π orbitals of CO also participate in electron donation to the metal

center (Scheme 10d), contrary to common knowledge. Nonetheless, the contribution of these orbitals to electron donation is much smaller than that of the σ orbital of CO.

As for the monocarbonyl pincer complexes, the competition between the C–H→Rh and CO→Rh electron donations is less pronounced than in the dicarbonyl systems, since the former are less electron-rich (only one CO ligand is available for σ donation). Therefore, the CO ligand in each of the monocarbonyl complexes experiences a smaller deviation from linearity than in the dicarbonyl complexes, with $\sphericalangle C_{ipso}$-Rh-$CO_{trans} \approx 170°$. Consequently, electron donation from CO to the d_{xz} orbital of rhodium is decreased, which results in less effective Rh→C–H back-donation. This, in turn, makes C–H bond cleavage less feasible than in the dicarbonyl systems, as it requires the C–H bond to approach the metal center more closely in the transition state. Indeed, the calculated geometries of the monocarbonyl transition states (see Tables 3, 8, and 9) display longer C–H bonds, as well as shorter Rh–C and Rh–H bonds, than the corresponding dicarbonyl systems (in other words, the monocarbonyl systems exhibit late transition states, whereas the dicarbonyl systems exhibit early ones). All in all, these differences in transition states lead to the kinetic preference for the CO-promotion pathway over the CO-trapping one.

Finally, a few words are in order regarding the transition state for C–H cleavage upon addition of acetonitrile to a monocarbonyl agostic complex. This reaction allows us to probe the role of σ donation in the absence of π back-donation, as acetonitrile is a good σ-donor, but a very weak π-acceptor. Thus, in contrast to CO, the π* orbitals of acetonitrile cannot effectively withdraw electron density from the Rh d_{z^2} orbital. On the other hand, the filled σ orbital of the acetonitrile molecule does interact with the metal center, injecting electron density into the Rh d_{z^2} orbital. This, in turn, leads to enhanced electronic repulsions along the arene-Rh-CO axis, which consequently inhibit C–H→Rh donation. Overall, the fact that the acetonitrile ligand inhibits the C–H→Rh donation, without countering this effect by bending or allowing for effective back-donation, results in a prohibitively high kinetic barrier for the acetonitrile-promoted pathway for C–H cleavage.

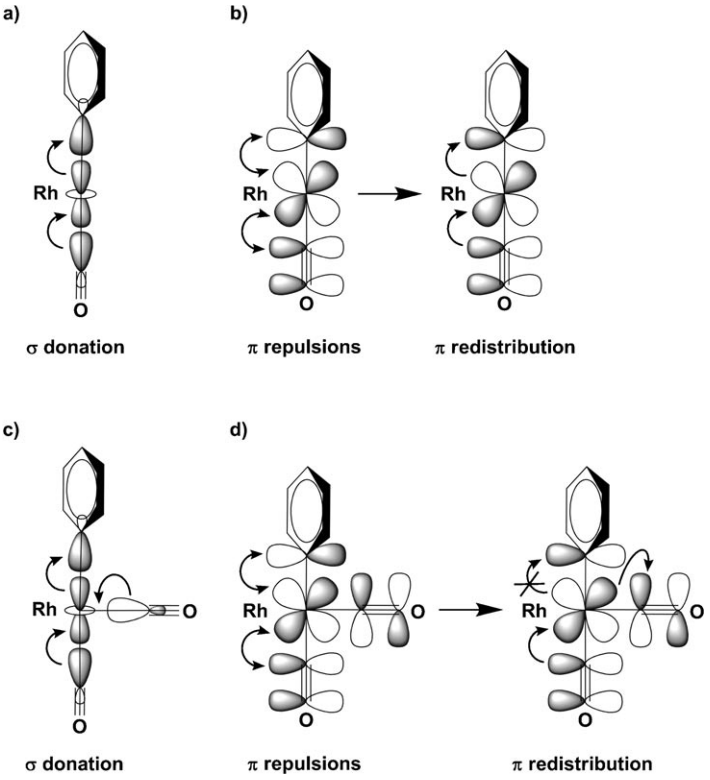

Scheme 11. Effect of a single *trans* CO ligand (a, b) and a combination of *trans* and *cis* CO ligands (c, d) on Rh–aryl bonding.

Aryl–hydrido complexes: The interactions of rhodium with the aryl and hydride ligands in the product of C–H oxidative addition determine the overall thermodynamics of this reaction. The important influence exerted by CO on these interactions is clearly demonstrated by both the experimental and theoretical results. Sigma donation from the CO ligand *trans* to the aryl moiety strongly enhances the Rh–C_{ipso} σ bonding, as depicted in Scheme 11a. For example, when the CO ligand in complex **9** was computationally removed, the overlap population of the Rh–C_{ipso} σ bond was found to decrease from 0.077 to 0.042. However, orbital population analysis also indicates that the same CO ligand significantly weakens the π interactions between the Rh atom and the aromatic ring in the aryl–hydrido complex. CDA demonstrates that in the absence of CO these interactions are at least as important as the σ bonding. The decreased Rh–C_{ipso} π interactions result from strong repulsions between the occupied π orbitals of CO, the Rh d_π orbitals, and the π system of the aromatic ring. This destabilizing *trans* influence forces partial charge transfer into the empty Rh–C_{ipso} π* orbital, so that the total Rh–aryl interaction within the π system becomes antibonding (Scheme 11b). Overall, the destabilizing effect of the *trans* CO ligand on the Rh–aryl π interaction is stronger than the stabilizing effect of σ donation. This is clearly manifested, for example, in the contraction of the computed Rh–C_{ipso} bond, from 2.049 to 1.970 Å, upon removal of the *trans* CO ligand from complex **9**. Moreover, the WBI for Rh–C_{ipso} increases dramatically from 0.41 to 0.81 upon removal of the CO ligand. As for the Rh–H interaction, our calculations show that it is only slightly affected by the presence of the CO ligand, which is positioned *cis* to the hydride ligand in the monocarbonyl aryl–hydrido complexes. Therefore, the electronic origin of the experimentally observed CO-induced reductive elimination of the C–H bonds in the PCP systems differs from the classical representation, which associates this type of reaction with a reduction in the electron density on the metal center as a result of the metal→CO back-donation. Instead, our results indicate that the key factor which leads to the CO-induced C–H reductive elimination is the repulsive interactions along the aryl-Rh-CO in the π system, which strongly destabilize the Rh–C_{ipso} bond.

In the dicarbonyl complexes, the CO ligand *cis* to the aryl moiety is more weakly bound to the metal center than the *trans* CO ligand (for example, the binding energies of these ligands in complex **4**, as estimated by CDA, are 33.3 and 41.3 kcal mol^{-1}, respectively). Unsurprisingly, the *cis* CO ligand exhibits weaker σ donation than the *trans* CO ligand (e.g., 0.34 vs. 0.43 electron in complex **4**), as well as weaker π back-donation (e.g., 0.25 vs. 0.28 electron in complex **4**). It is important to note that the extent of π back-donation, relative to σ donation, is higher for the *cis* CO ligand, and this feature underlies the unusual effect of this ligand in promoting C–H oxidative addition. The charge transfer from Rh to *cis* CO reduces the repulsion between the occupied d_π orbitals of Rh and the occupied π orbitals of both the aryl moiety and the *trans* CO ligand. This is accomplished by directing the excess electron density, which originates from this repulsion, to the π* orbital of *cis* CO instead of the Rh–C_{ipso} π* orbital (Scheme 11d). This distribution of electron density lowers the energy of the aryl–hydrido complexes and assists the oxidative addition reaction.

The existence of repulsive π interactions along the C_{ipso}-Rh-CO axis, which accounts for C–H reductive elimination upon addition of a single CO ligand to the PCP-based aryl–hydrido complexes, can also account for the surprising stability of the POCOP-based aryl–hydrido–carbonyl complexes. In fact, the higher electrophilicity of the POCOP ligand, as compared with PCP, which was initially thought to hinder the formation of an aryl–hydrido–monocarbonyl complex, actually serves to stabilize this structure. Thus, analysis of the electronic structure of the POCOP complexes reveals that the relatively high electrophilicity of the ligand effectively redistributes the excessive electron density that accumulates in the aryl moiety upon addition of CO to the aryl–hydrido complex, thereby significantly reducing the repulsive Rh–C_{ipso} interactions (Scheme 12). The pronounced electronic effect of the POCOP ligand is clearly evident by comparing the natural population analysis (NPA) charges on various atoms in its relevant complexes. Thus, the carbon atoms *ortho* to C_{ipso} experience a decrease of positive charge from +0.61 in complex **18** to +0.48 in complex **15**, whereas the negative charge on the oxygen atoms of the POCOP ligand increases from −0.77 to −0.80, respectively. This leads to a significant decrease in the total electron density on C_{ipso} upon C–H oxidative addition (i.e., the reaction **18**→**15**), with its natural charge dropping from −0.82 to −0.68. Similar electronic redistributions in the PCP systems are much more subtle. For example, the natural charge on C_{ipso} changes from −0.52 to −0.45 on going from complex **7** to **11**, respectively.

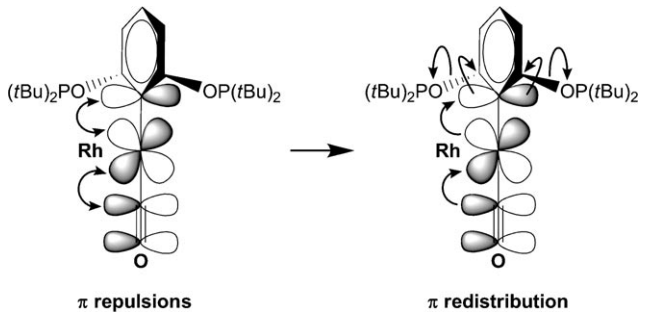

Scheme 12. Repulsive π interactions in the POCOP complexes.

As for the role of acetonitrile in promoting C–H oxidative addition in the agostic complex, it was found that the nitrile ligand assists this reaction by stabilizing the resulting Rh–H bond, in contrast to the CO ligand, which promotes this reaction by reducing the Rh–aryl repulsion. A comparison of the electronic structures of acetonitrile–carbonyl complex **20** and dicarbonyl complex **4** reveals that the Rh–H bond in complex **20** is significantly more stable than in complex **4**, as reflected by their calculated metal–hydride bond lengths (1.533 Å for **20** vs. 1.573 Å for **4**), as well as by the Wiberg bond indexes (0.589 for **20** vs. 0.435 for **4**). On the other hand, the acetonitrile ligand in complex **20** is bound much more weakly than *cis* CO in complex **4**, with binding energies of 4.0 and 10.6 kcal mol^{-1}, respectively. CDA reveals that this difference in binding energy arises from the absence of π interactions between rhodium and the acetonitrile ligand, as well as relatively weak σ donation from this ligand to the electron-rich metal center.

Conclusion

In this work we have explored the effects of CO on the oxidative addition of strong arene C–H bonds in cationic pincer-type complexes of rhodium. This investigation revealed intriguing, even counterintuitive processes involving this ubiquitous simple ligand.

Firstly, we demonstrated that in cationic, phosphine-based, PCP-type pincer complexes of rhodium, CO exhibits a dual role as far as C–H activation is concerned. Thus, when one molecule of CO was added to a solvent-stabilized aryl–hydrido Rh^{III} complex, C–H reductive elimination ensued, thereby affording the corresponding C–H agostic monocarbonyl Rh^{I} complex. This is the expected manifestation of the well-known character of CO as a strong π-accepting ligand. However, when a second molecule of CO was added to the agostic complex, C–H oxidative addition took place, thereby yielding the corresponding aryl–hydrido dicarbonyl Rh^{III} complex. This result stands in contradiction to the traditional view of CO as a predominantly π-accepting ligand, and indicates that in the present systems CO can behave as a significant σ-donor. Indeed, DFT analysis of these systems strongly supported the notion that CO acts primarily as a σ-donor, a property that is likely applicable to cationic late-transition-metal complexes in general. Nonetheless, the most important effect of CO in the presently studied systems was actually attributed to its filled π orbitals. Thus, when the first CO molecule binds to the aryl–hydrido Rh^{III} complex, its coordination *trans* to the aryl moiety leads to strong π–π repulsion along the aryl-Rh-CO

axis. This repulsion destabilizes the aryl–hydrido complex and favors C–H reductive elimination. Addition of a second CO ligand in the position *cis* to the aryl ligand reduces this unfavorable effect by transferring excess electron density into the π* orbitals of the additional carbonyl ligand.

Secondly, we showed that when the phosphine-based PCP-type ligand is replaced by a phosphinite-based POCOP-type ligand, the reactivity of the system changes significantly. Thus, it was found that addition of one molecule of CO to a solvent-stabilized aryl–hydrido Rh^{III} complex of the POCOP ligand does not lead to C–H reductive elimination, but instead affords a relatively stable CO adduct of this aryl–hydrido complex. Addition of a second CO molecule to the monocarbonyl aryl–hydrido complex leads to the corresponding aryl–hydrido dicarbonyl Rh^{III} species, as also observed for the PCP systems. These results were corroborated by DFT calculations, which also indicated that the different behavior of the POCOP system, relative to the PCP system, originates from the higher electrophilicity of the POCOP ligand, which counteracts the repulsive π–π interactions along the aryl-Rh-CO axis. Furthermore, the DFT analysis exposed the important role of the BF_4^- counterion in the stabilization of the monocarbonyl aryl–hydrido complex, and also accounted for the observed elimination of HBF_4 from this complex, which was attributed to the formation of an unobserved acidic agostic complex.

Finally, the effects of CO on the PCP system were compared with that of acetonitrile, which is commonly accepted as a σ-donor with a negligible π-acceptor character. Interestingly, acetonitrile was found to react with an agostic monocarbonyl Rh^{I} complex in much the same way as CO, thus leading to the corresponding aryl–hydrido Rh^{III} complex. Nonetheless, our DFT results indicate that unlike CO, acetonitrile does not promote C–H oxidative addition, but merely acts as a trapping agent. The fact that the direct promotion pathway is essentially blocked for acetonitrile is linked to its inability to engage in π interactions with the metal center, thereby preventing it from reducing the electronic repulsions that develop in the transition state prior to C–H cleavage.

Experimental Section

General procedures: All experiments with metal complexes and the phosphine ligands were carried out under an atmosphere of purified nitrogen in an MBraun MB 150B-G glove box or an atmosphere of purified argon in an MBraun Unilab glove box. All solvents were reagent grade or better. All nondeuterated solvents were heated at reflux over sodium/benzophenone ketyl and distilled under an argon atmosphere. Deuterated solvents were used as received. All the solvents were degassed with argon or nitrogen and kept in the glove box over 3 or 4 Å molecular sieves (except for acetone, which was dried with Drierite). Commercially available reagents were used as received. The complex $[Rh(acetone)_2(coe)_2]BF_4$ was prepared according to a literature procedure with appropriate modifications.[45] Ligand **1** and complexes **2**, **3**, and **4** were prepared as previously reported.[7] Ligands **5**[46] and **13**[25a] were synthesized according to literature procedures. Crystal structures were drawn using the program ORTEP-3.[47]

Analysis: NMR spectra (^1H, ^{13}C, ^{19}F, and ^{31}P) were recorded using Bruker Avance 250, Bruker Avance 400, or Bruker Avance 500 NMR spectrometers. All measurements were done at 20 °C unless otherwise noted. ^1H and ^{13}C NMR chemical shifts are reported in ppm relative to tetramethylsilane. ^1H NMR chemical shifts are referenced to the residual hydrogen signal of the deuterated solvents, and the ^{13}C NMR chemical shifts are referenced to the ^{13}C signal(s) of the deuterated solvents. ^{19}F NMR chemical shifts are reported in ppm relative to $CFCl_3$ and referenced to an external solution of C_6F_6 in $CDCl_3$. ^{31}P NMR chemical shifts are reported in ppm relative to H_3PO_4 and referenced to an external 85% solution of phosphoric acid in D_2O. Abbreviations used in the description of NMR data are as follows: Ar, aryl; br, broad; v, virtual; s, singlet; d, doublet; t, triplet; m, multiplet. Infrared spectra were recorded using Nicolet Protégé 460 and Nicolet 6700 FTIR spectrometers. Such spectra are reported only for those complexes that were isolable and stable at room temperature (compounds **17** and **20**). Elemental analyses were performed at the Chemical Analysis Laboratory (Department of Chemical Research Support), Weizmann Institute of Science, and at H. Kolbe Mikroanalytisches Laboratorium, Mülheim an der Ruhr, Germany.

Crystal structures from the Cambridge Structural Database (CSD; version 5.29, November 2007)[48,49] were retrieved and analyzed using ConQuest 1.10[50] and Vista,[51] respectively. In order to avoid redundant crystal structures during the database search, we have used the best representative polymorph list supplied by the Cambridge Crystallographic Data Centre (CCDC).[52]

X-ray crystallographic analysis: Data were collected as ϕ and ω scans using a Nonius KappaCCD diffractometer at 120(2) K, with $Mo_{K\alpha}$ radiation ($\lambda = 0.71073$ Å) and a graphite monochromator. Data processing was carried out with Denzo-Scalepack.[53] Structures were solved by direct methods with SHELXS-97[54] and SIR-97,[55] and refined with SHELXL-97[54] using the full-matrix least-squares method based on F^2. Hydrogen atoms were placed in calculated positions and refined in riding mode, unless otherwise noted.

Reaction of $[Rh(acetone)_2(coe)_2]BF_4$ with ligand 5—formation of complex 6: A solution of ligand **5** (39.1 mg, 0.099 mmol) in acetone (1.3 mL) was added to a solution of $[Rh(acetone)_2(coe)_2]BF_4$ (52.2 mg, 0.099 mmol) in acetone (1.3 mL). The resulting solution rapidly changed from orange to yellow as it was stirred at room temperature. After 1.5 h the volume of solution was reduced under vacuum to 0.6 mL and it was then added to pentane (13 mL), with stirring, to precipitate the product. The pentane phase was then decanted and the product was washed with pentane (2 mL) and dried under vacuum to afford 53.0 mg (0.083 mmol, 83.3% yield) of the product as a yellow powder. $^{31}P\{^1H\}$ NMR (202 MHz, $CDCl_3$): $\delta = 77.51$ ppm (d, $^1J(Rh,P) = 115.9$ Hz); ^1H NMR (500 MHz, $CDCl_3$): $\delta = 6.93$ (d, $^3J(H,H) = 7.4$ Hz, 2H; *meta* Ar-*H*), 6.86 (t, $^3J(H,H) = 7.4$ Hz, 1H; *para* Ar-*H*), 3.23 (dvt, $^2J(H,H) = 17.2$ Hz, $^2J(P,H)+{}^4J(P,H) = 7.0$ Hz, 2H; Ar-CH_2-P, downfield part of ABX-system), 3.15 (dvt, $^2J(H,H) = 17.5$ Hz, $^2J(P,H)+{}^4J(P,H) = 8.0$ Hz, 2H; Ar-CH_2-P, upfield part of ABX-system), 2.31 (s, 6H; coordinated O=C(CH_3)$_2$), 1.34 (vt, $^3J(P,H)+{}^5J(P,H) = 13.8$ Hz, 36H; PC(CH_3)$_3$), −27.48 ppm (dt, $^1J(Rh,H) = 59.0$ Hz, $^2J(P,H) = 10.8$ Hz, 1H; Rh-*H*); $^{13}C\{^1H\}$ NMR (126 MHz, $CDCl_3$): $\delta = 151.64$ (vt, $^2J(P,C)+{}^4J(P,C) = 17.8$ Hz; C_{Ar}-CH_2-P), 147.43 (br d, $^1J(Rh,C) = 37.3$ Hz; C_{ipso}), 125.04 (s, C_{Ar}-H), 123.43 (vt, $^3J(P,C)+{}^5J(P,C) = 17.4$ Hz; C_{Ar}-H), 36.21 (vt, $^1J(P,C)+{}^3J(P,C) = 15.6$ Hz; P$C(CH_3)_3$), 34.16 (vtd, $^1J(P,C)+{}^3J(P,C) = 18.6$ Hz, $^2J(Rh,C) = 1.3$ Hz; P$C(CH_3)_3$), 31.85 (br s, coordinated O=$C(CH_3)_2$), 30.85 (vtd, $^1J(P,C)+{}^3J(P,C) = 23.6$ Hz, $^2J(Rh,C) = 3.3$ Hz; C_{Ar}-CH_2-P), 29.61 (vt, $^2J(P,C)+{}^4J(P,C) = 5.2$ Hz; PC-(CH_3)$_3$), 28.96 ppm (vt, $^2J(P,C)+{}^4J(P,C) = 4.8$ Hz; PC(CH_3)$_3$); $^{19}F\{^1H\}$ NMR (376 MHz, $CDCl_3$): $\delta = -167.0$ (very broad singlet, BF_4); $^{31}P\{^1H\}$ NMR (202 MHz, [D$_6$]acetone): $\delta = 79.20$ ppm (d, $^1J(Rh,P) = 116.3$ Hz); ^1H NMR (500 MHz, [D$_6$]acetone): $\delta = 6.92$ (d, $^3J(H,H) = 7.4$ Hz, 2H; *meta* Ar-*H*), 6.82 (m, $^3J(H,H) = 7.4$ Hz, 1H; *para* Ar-*H*), 3.37 (dvt, $^2J(H,H) = 17.1$ Hz, $^2J(P,H)+{}^4J(P,H) = 6.8$ Hz, 2H; Ar-CH_2-P, downfield part of ABX-system), 3.31 (dvt, $^2J(H,H) = 17.1$ Hz, $^2J(P,H)+{}^4J(P,H) = 8.4$ Hz, 2H; Ar-CH_2-P, upfield part of ABX-system), 2.08 (s,

6H; free O=C(CH_3)$_2$), 1.31 (vt, 18H; PC(CH_3)$_3$), 1.28 (vt, 18H; PC(CH_3)$_3$), −22.84 ppm (br d, ^1J(Rh,H) = 34.0 Hz, 1H; Rh-*H*); elemental analysis calcd (%) for $C_{24}H_{44}BF_4P_2Rh$ (no acetone molecules present): C 49.34, H 7.59; found: C 49.36, H 8.02.

Reaction of complex 6 with CO—in situ synthesis of agostic complex 7 and aryl–hydrido complex 8: Complex **6** (31.1 mg, 0.048 mmol) was dissolved in $CDCl_3$ (0.6 mL) and the resulting solution was loaded into a screw-cap NMR tube. The tube was fitted with a rubber septum and then CO was bubbled freely through the solution, via a syringe, for 2 min (the NMR tube was kept open during bubbling by using a second syringe as a gas outlet in order to prevent over-pressure of CO). The resulting solution (under an atmosphere of CO) was then analyzed by NMR spectroscopy at −40 °C, since complex **8** is only observed at low temperatures. Moreover, the solution contained a mixture of complexes **7** and **8**. The full characterization of complex **7** at room temperature has been reported previously,[11a] but selected low-temperature data are also given here for comparative purposes.

Complex ***7***: $^{31}P\{^1H\}$ NMR (162 MHz, $CDCl_3$, −40 °C): δ = 34.66 ppm (d, ^1J(Rh,P) = 100.1 Hz); ^{1}H NMR (400 MHz, $CDCl_3$, −40 °C): δ = 7.61 (t, ^3J(H,H) = 7.6 Hz, 1H; *para*-Ar-*H*), 7.22 (d, ^3J(H,H) = 7.2 Hz, 2H; *meta*-Ar-*H*), 3.98 (d, ^1J(Rh,H) = 18.4 Hz, 1H; agostic C-*H*), 3.76 (dt, ^2J(H,H) = 16.3 Hz, ^2J(P,H) = 4.7 Hz, 2H; ArCH_2P, downfield part of ABX system), 3.30 (dt, ^2J(H,H) = 16.3 Hz, ^2J(P,H) = 2.9 Hz, 2H; ArCH_2P, upfield part of ABX system), 1.40 (vt, ^3J(P,H)+^5J(P,H) = 15.0 Hz, 18H; PC(CH_3)$_3$), 1.19 ppm (vt, ^3J(P,H)+^5J(P,H) = 14.6 Hz, 18H; PC(CH_3)$_3$); selected $^{13}C\{^1H\}$ NMR (101 MHz, $CDCl_3$, −40 °C): δ = 188.69 ppm (dt, ^1J(Rh,C) = 90.6 Hz, ^2J(P,C) = 11.6 Hz; *C*O).

Complex ***8***: $^{31}P\{^1H\}$ NMR (162 MHz, $CDCl_3$, −40 °C): δ = 98.13 ppm (d, ^1J(Rh,P) = 89.9 Hz); ^{1}H NMR (400 MHz, $CDCl_3$, −40 °C): δ = 7.09 (d, ^3J(H,H) = 7.5 Hz, 2H; *meta* Ar-*H*), 6.95 (t, ^3J(H,H) = 7.5 Hz, 1H; *para*-Ar-*H*), 3.51 (m, 4H; Ar-CH_2-P), 1.47 (vt, ^3J(P,H)+^5J(P,H) = 15.2 Hz, 18H; PC(CH_3)$_3$), 1.26 (m, 18H; PC(CH_3)$_3$), −8.95 ppm (dt, ^1J(Rh,H) = 11.6 Hz, ^2J(P,H) = 3.5 Hz, 1H; Rh-*H*); $^{13}C\{^1H\}$ NMR (101 MHz, $CDCl_3$, −40 °C): δ = 186.86 (m, ^1J(Rh,C) = 40.7 Hz; *C*O *trans* to hydride), 185.59 (dt, ^1J(Rh,C) = 42.8 Hz, ^2J(P,C) = 9.2 Hz; *C*O *trans* to aryl), 149.98 (d, ^1J(Rh,C) = 22.5 Hz; C_{ipso}), 147.05 (vt, ^2J(P,C)+^4J(P,C) = 13.0 Hz; Ar_{ortho}), 127.13 (s; Ar_{para}), 124.08 (vt, ^3J(P,C)+^5J(P,C) = 17.4 Hz; Ar_{meta}), 37.63 (vt, ^1J(P,C)+^3J(P,C) = 21.0 Hz; P*C*(CH$_3$)$_3$), 36.82 (vt, ^1J(P,C)+^3J(P,C) = 17.8 Hz; P*C*(CH$_3$)$_3$), 35.96 (vt, ^1J(P,C)+^3J(P,C) = 25.0 Hz; Ar*C*H$_2$P), 29.70 (s; PC(CH_3)$_3$), 28.76 ppm (s; PC(*C*H$_3$)$_3$); ^{19}F NMR (376 MHz, $CDCl_3$, −40 °C): δ = −153.18 ppm (s; BF_4).

Synthesis of complexes 7 and 8 with ^{13}C-labeled CO: Complex **6** (3.5 mg, 0.005 mmol) was dissolved in $CDCl_3$ (0.6 mL) and the resulting solution was treated with ^{13}CO (99 atom % ^{13}C). This reaction was carried out in a manner identical to the above-mentioned synthesis of unlabeled **7** and **8** using regular CO.

Complex ***7-^{13}CO*** *(selected signals)*: $^{31}P\{^1H\}$ NMR (162 MHz, $CDCl_3$, −40 °C): δ = 34.56 ppm (dd, ^1J(Rh,P) = 100.2 Hz, ^2J(C,P) = 11.6 Hz); selected ^{1}H NMR (400 MHz, $CDCl_3$, −40 °C): δ = 4.15 ppm (m, ^1J(Rh,H) = 17.9 Hz, ^2J(C,H) = 5.5 Hz, 1H; agostic C-*H*); selected ^{13}C NMR (101 MHz, $CDCl_3$, −40 °C): δ = 188.68 ppm (dtd, ^1J(Rh,C) = 90.6 Hz, ^2J(P,C) = 11.5 Hz, ^2J(H,C) = 6.1 Hz; *C*O).

Complex ***8-^{13}CO*** *(selected signals)*: $^{31}P\{^1H\}$ NMR (162 MHz, $CDCl_3$, −40 °C): δ = 97.99 ppm (ddd, ^1J(Rh,P) = 90.0 Hz, ^2J(C,P) = 9.0 Hz, ^2J(C,P) = 6.3 Hz); selected ^{1}H NMR (400 MHz, $CDCl_3$, −40 °C): δ = −8.96 ppm (m, ^1J(Rh,H) = 11.6 Hz, ^2J(C,H) = 59.6 Hz, ^2J(C,H) = 4.8 Hz, 1H; Rh-*H*); selected ^{13}C NMR (101 MHz, $CDCl_3$, −40 °C): δ = 186.83 (m, ^1J(Rh,C) = 39.5 Hz, ^2J(H,C) = 59.7 Hz; *C*O *trans* to hydride), 185.55 ppm (m, ^1J(Rh,C) = 43.0 Hz, ^2J(H,C) = 4.8 Hz; *C*O *trans* to aryl).

Reaction of [Rh(acetone)$_2$(CO)$_2$]BF$_4$ with ligand 5 in [D$_6$]acetone—direct formation of 7 and 8: A solution of $AgBF_4$ (5.6 mg, 0.029 mmol) in [D$_6$]acetone (0.23 mL) was added dropwise to a stirring solution of [{Rh(CO)$_2$Cl}$_2$] (5.6 mg, 0.014 mmol) in [D$_6$]acetone (0.23 mL). The resulting mixture was stirred for 15 min in the dark, at room temperature, and then filtered through a cotton pad to remove the AgCl precipitate and afford a clear, pale yellow solution. A solution of ligand **5** was then prepared by dissolving the ligand (11.2 mg, 0.028 mmol) in [D$_6$]acetone (0.34 mL). The solution containing [Rh(acetone)$_2$(CO)$_2$]BF$_4$ was loaded into an NMR tube fitted with a rubber septum, and then cooled to −78 °C in a bath of dry ice and acetone. The solution of ligand **5** was then injected into the NMR tube and the two solutions were quickly mixed by shaking the NMR tube, and then reintroduced into the bath of dry ice and acetone for a few minutes. The resulting solution was then transferred to the NMR spectrometer, which had been precooled to −70 °C, for examination.

Synthesis of pure complex 7: A solution of ligand **5** (22.7 mg (0.057 mmol) in acetone (0.5 mL) was added to a solution of [Rh(acetone)$_2$(coe)$_2$]BF$_4$ (30.0 mg, 0.057 mmol) in acetone (0.5 mL). The solution was stirred at room temperature for 2 h and then CO (1.5 mL, 0.062 mmol) was bubbled through the solution (the reaction vessel was kept closed by a rubber septum in order to prevent loss of CO gas). The excess CO was then pumped off and pentane (3 mL) was added to the solution. The resulting suspension was stored overnight at −35 °C to facilitate the precipitation of the product. The liquid phase was then decanted and the product was washed with pentane (18 mL) and dried under vacuum. This afforded the product as a fine yellow powder (26.1 mg, 0.043 mmol, 74.8 % yield). The triflate analogue of this complex has been fully characterized in a previous publication.[11a]

Reaction of [Rh(acetone)$_2$(coe)$_2$]BF$_4$ with ligand 13—formation of complex 14: A solution of ligand **13** (99.2 mg, 0.249 mmol) in acetone (1.8 mL) was added to a solution of [Rh(acetone)$_2$(coe)$_2$]BF$_4$ (130.8 mg, 0.249 mmol) in acetone (2.7 mL). The resulting solution was stirred at room temperature for 1.5 h. The volume of this solution was then reduced under vacuum to about 1 mL and the concentrated solution was added to pentane (14.5 mL), with stirring, to precipitate the product. The liquid phase was then decanted and the product was washed with pentane (5.5 mL) and dried under vacuum to afford the product as a yellow powder (147.0 mg, 0.227 mmol, 91.5 % yield). $^{31}P\{^1H\}$ NMR (202 MHz, $CDCl_3$): δ = 189.42 ppm (d, ^1J(Rh,P) = 122.4 Hz); ^{1}H NMR (500 MHz, $CDCl_3$): δ = 6.94 (t, ^3J(H,H) = 8.0 Hz, 1H; *para* Ar-*H*), 6.53 (d, ^3J(H,H) = 8.0 Hz, 2H; *meta* Ar-*H*), 2.30 (s, 6H; coordinated O=C(CH_3)$_2$), 1.35 (vt, 18H; PC(CH_3)$_3$), 1.34 (vt, 18H; PC(CH_3)$_3$), −26.87 ppm (dt, ^1J(Rh,H) = 53.8 Hz, ^2J(P,H) = 9.7 Hz, 1H; Rh-*H*); $^{13}C\{^1H\}$ NMR (126 MHz, $CDCl_3$): δ = 167.63 (vt, ^2J(P,C)+^4J(P,C) = 11.8 Hz; C_{Ar}-O-P), 128.12 (s; C_{Ar}-H), 117.86 (br d, ^1J(Rh,C) = 35.6 Hz; C_{ipso}), 106.82 (vt, ^3J(P,C)+^5J(P,C) = 11.4 Hz; C_{Ar}-H), 41.12 (vt, ^1J(P,C)+^3J(P,C) = 16.6 Hz; P*C*(CH$_3$)$_3$), 38.40 (vtd, ^1J(P,C)+^3J(P,C) = 20.2 Hz, ^2J(Rh,C) = 2.3 Hz; P*C*(CH$_3$)$_3$), 31.78 (s; coordinated O=*C*(CH$_3$)$_2$), 27.57 (vt, ^2J(P,C)+^4J(P,C) = 7.2 Hz; PC(CH_3)$_3$), 27.27 ppm (vt, ^2J(P,C)+^4J(P,C) = 6.8 Hz; PC(CH_3)$_3$); $^{19}F\{^1H\}$ NMR (376 MHz, $CDCl_3$): δ = −165.4 (very broad singlet, BF_4); $^{31}P\{^1H\}$ NMR (202 MHz, [D$_6$]acetone): δ = 189.67 ppm (d, ^1J(Rh,P) = 119.6 Hz); ^{1}H NMR (500 MHz, [D$_6$]acetone): δ = 7.09 (t, ^3J(H,H) = 8.1 Hz, 1H; *meta*-Ar-*H*), 6.69 (d, ^3J(H,H) = 8.1 Hz, 2H; *para*-Ar-*H*), 2.08 (s, 6H; free O=C(CH_3)$_2$), 1.38 (m, 36H; PC(CH_3)$_3$), −26.18 ppm (dt, ^1J(Rh,H) = 52.9 Hz, ^2J(P,H) = 9.9 Hz, 1H; Rh-*H*); elemental analysis calcd (%) for $C_{25}H_{46}BF_4O_3P_2Rh$ (one acetone molecule present): C 46.46, H 7.17; found: C 46.39, H 7.28.

Reaction of 14 with CO—in situ formation of complexes 15 and 16: Complex **14** (34.6 mg, 0.054 mmol) was dissolved in $CDCl_3$ (1.5 mL) and loaded into an NMR tube fitted with a rubber septum. The solution was then cooled to −20 °C (dry ice/acetone bath) and CO (1.2 mL, 0.050 mmol) was bubbled through the solution via a syringe (the NMR tube was kept closed by the rubber septum in order to prevent loss of CO gas). The sample was then transferred to the NMR spectrometer, which was precooled to −40 °C, for the low-temperature characterization of complex **15** (80 % yield, based on the $^{31}P\{^1H\}$ NMR spectrum). After completion of measurements (4 h), the sample was transferred back to the bath of dry ice and acetone (−20 °C) and CO gas was freely bubbled through the solution, via a syringe, for 1 min (the system was kept open during bubbling by using a second syringe as a gas outlet, in order to prevent over-pressure of CO). The sample was then transferred to the NMR spectrometer, which was precooled to −40 °C, for the low-temperature characterization of complex **16** (98 % yield, relative to starting material, based on the $^{31}P\{^1H\}$ NMR spectrum). For comparative purposes, the preparation of both complexes was also carried out at room temperature, using similar methodology.

Complex ***15***: $^{31}P\{^1H\}$ NMR (162 MHz, $CDCl_3$, −40 °C): δ = 203.59 ppm (d, $^1J(Rh,P)$ = 105.7 Hz); ^1H NMR (400 MHz, $CDCl_3$, −40 °C): δ = 7.57 (t, $^3J(H,H)$ = 8.2 Hz, 1H; *para* Ar-*H*), 6.85 (d, $^3J(H,H)$ = 8.2 Hz, 2H; *meta* Ar-*H*), 1.36 (m, 18H; $PC(CH_3)_3$), 1.30 (m, 18H; $PC(CH_3)_3$), −12.36 ppm (d, $^1J(Rh,H)$ = 40.8 Hz, 1H; Rh-*H*); $^{13}C\{^1H\}$ NMR (101 MHz, $CDCl_3$, −40 °C): δ = 188.50 (dt, $^1J(Rh,C)$ = 63.5 Hz, $^2J(P,C)$ = 9.1 Hz; *C*O), 170.35 (vt, $^2J(P,C)+^4J(P,C)$ = 9.2 Hz; C_{Ar}-O-P), 139.02 (s; C_{Ar}-H), 115.34 (m; C_{ipso}), 109.64 (vt, $^3J(P,C)+^5J(P,C)$ = 10.2 Hz; C_{Ar}-H), 42.33 (vt, $^1J(P,C)+^3J(P,C)$ = 16.8 Hz; P*C*$(CH_3)_3$), 39.65 (vtd, $^1J(P,C)+^3J(P,C)$ = 19.8 Hz, $^2J(Rh,C)$ = 2.1 Hz; P*C*$(CH_3)_3$), 27.84 (s, P*C*$(CH_3)_3$), 27.36 ppm (s; PC-*C*$H_3)_3$); $^{19}F\{^1H\}$ NMR (376 MHz, $CDCl_3$, −40 °C): δ = −152.48 ppm (br s; BF_4); $^{31}P\{^1H\}$ NMR (202 MHz, $CDCl_3$, 20 °C): δ = 203.76 ppm (d, $^1J(Rh,P)$ = 105.8 Hz). ^1H NMR (500 MHz, $CDCl_3$, 20 °C): δ = 7.56 (t, $^3J(H,H)$ = 7.9 Hz, 1H; *para* Ar-*H*), 6.87 (d, $^3J(H,H)$ = 8.0 Hz, 2H; *meta* Ar-*H*), 1.39 (m, 18H; $PC(CH_3)_3$), 1.34 (m, 18H; $PC(CH_3)_3$), −12.88 ppm (d, $^1J(Rh,H)$ = 41.1 Hz, 1H; Rh-*H*).

Complex ***16***: $^{31}P\{^1H\}$ NMR (162 MHz, $CDCl_3$, −40 °C): δ = 209.96 ppm (d, $^1J(Rh,P)$ = 93.5 Hz); ^1H NMR (400 MHz, $CDCl_3$, −40 °C): δ = 7.02 (t, $^3J(H,H)$ = 8.0 Hz, 1H; *para* Ar-*H*), 6.65 (d, $^3J(H,H)$ = 8.1 Hz, 2H; *meta* Ar-*H*), 1.53 (vt, $^3J(P,H)+^5J(P,H)$ = 16.8 Hz, 18H; $PC(CH_3)_3$), 1.30 (vt, $^3J(P,H)+^5J(P,H)$ = 15.8 Hz, 18H; $PC(CH_3)_3$), −9.58 ppm (m, $^1J(Rh,H)$ = 10.3 Hz, 1H; Rh-*H*); $^{13}C\{^1H\}$ NMR (101 MHz, $CDCl_3$, −40 °C): δ = 184.55 (m, $^1J(Rh,C)$ = 37.4 Hz; *C*O *trans* to hydride), 182.19 (dt, $^1J(Rh,C)$ = 45.7 Hz, $^2J(P,C)$ = 6.7 Hz; *C*O *trans* to aryl), 162.84 (vt, $^2J(P,C)+^4J(P,C)$ = 7.8 Hz; C_{Ar}-O-P), 129.63 (s; C_{Ar}-H), 122.78 (dt, $^1J(Rh,C)$ = 22.6 Hz, $^2J(P,C)$ = 4.4 Hz; C_{ipso}), 107.97 (vt, $^3J(P,C)+^5J(P,C)$ = 11.2 Hz; C_{Ar}-H), 43.08 (vtd, $^1J(P,C)+^3J(P,C)$ = 19.4 Hz, $^2J(Rh,C)$ = 2.5 Hz; P*C*$(CH_3)_3$), 41.14 (vt, $^1J(P,C)+^3J(P,C)$ = 20.0 Hz; P*C*$(CH_3)_3$), 28.12 (s; PC-*C*$H_3)_3$), 27.68 ppm (s; $PC(CH_3)_3$); $^{19}F\{^1H\}$ NMR (376 MHz, $CDCl_3$, −40 °C): δ = −150.95 ppm (s; BF_4); $^{31}P\{^1H\}$ NMR (202 MHz, $CDCl_3$, 20 °C): δ = 210.52 ppm (d, $^1J(Rh,P)$ = 93.6 Hz); ^1H NMR (500 MHz, $CDCl_3$, 20 °C): δ = 7.04 (t, $^3J(H,H)$ = 8.0 Hz, 1H; *para*-Ar-*H*), 6.67 (d, $^3J(H,H)$ = 8.1 Hz, 2H; *meta*-Ar-*H*), 1.57 (vt, $^3J(P,H)+^5J(P,H)$ = 16.8 Hz, 18H; $PC(CH_3)_3$), 1.34 (vt, $^3J(P,H)+^5J(P,H)$ = 16.2 Hz, 18H; $PC(CH_3)_3$), −9.53 ppm (m, 1H; Rh-*H*).

Synthesis of complexes 15 and 16 with ^{13}C-labeled CO: Complex **14** (2.1 mg, 0.003 mmol) was dissolved in $CDCl_3$ (0.6 mL) and the resulting solution was treated with ^{13}CO (99 atom % ^{13}C). This reaction was carried out in a manner identical to the above-mentioned synthesis of unlabeled **15** and **16** using regular CO.

Complex ***15-^{13}CO*** *(selected signals)*:[56] $^{31}P\{^1H\}$ NMR (162 MHz, $CDCl_3$, −40 °C): δ = 204.36 ppm (dd, $^1J(Rh,P)$ = 105.3 Hz, $^2J(C,P)$ = 8.5 Hz); selected ^1H NMR (400 MHz, $CDCl_3$, −40 °C): δ = −14.96 ppm (br d, $^1J(Rh,H)$ = 43.6 Hz, 1H; Rh-*H*); selected ^{13}C NMR (101 MHz, $CDCl_3$, −40 °C): δ = 188.58 ppm (dt, $^1J(Rh,C)$ = 60.1 Hz, $^2J(P,C)$ = 8.5 Hz; *C*O).

Complex ***16-^{13}CO*** *(selected signals)*: $^{31}P\{^1H\}$ NMR (162 MHz, $CDCl_3$, −40 °C): δ = 209.89 ppm (dt, $^1J(Rh,P)$ = 93.7 Hz, $^2J(C,P)$ = 6.7 Hz); selected ^1H NMR (400 MHz, $CDCl_3$, −40 °C): δ = −9.63 ppm (br d, $^2J(C,H)$ = 62.3 Hz, 1H; Rh-*H*); selected ^{13}C NMR (101 MHz, $CDCl_3$, −40 °C): δ = 184.53 (m, $^1J(Rh,C)$ = 39.2 Hz, $^2J(H,C)$ = 63.3 Hz; *C*O *trans* to hydride), 182.10 ppm (m, $^1J(Rh,C)$ = 45.7 Hz; *C*O *trans* to aryl).

Synthesis of complex 17: Under an atmosphere of dry nitrogen, a solution of KO*t*Bu (6.8 mg, 0.061 mmol) in THF (0.6 mL) was added to a solution of **14** (34.0 mg, 0.053 mmol) in THF (1.2 mL). The resulting solution was stirred at room temperature for 45 min. The reaction vessel was then fitted with a rubber septum and CO was bubbled through the solution, via a syringe, for 2 min (the system was kept open during bubbling by using a second syringe as a gas outlet, in order to prevent over-pressure of CO). The solvent was then removed under vacuum and the residue was extracted with benzene (3.0 mL). The resulting yellow solution was passed through a cotton filter, frozen at −35 °C, and the solvent was then removed by sublimation under vacuum. This resulted in the product as a fine yellow powder (20.0 mg, 0.038 mmol, 71.9 % yield). $^{31}P\{^1H\}$ NMR (202 MHz, C_6D_6): δ = 215.13 ppm (d, $^1J(Rh,P)$ = 156.9 Hz); ^1H NMR (500 MHz, C_6D_6): δ = 6.94 (t, $^3J(H,H)$ = 7.9 Hz, 1H; *para*-Ar-*H*), 6.81 (d, $^3J(H,H)$ = 7.9 Hz, 2H; *meta*-Ar-*H*), 1.28 ppm (vt, $^3J(P,H)+^5J(P,H)$ = 14.2 Hz, 36H; $PC(CH_3)_3$); $^{13}C\{^1H\}$ NMR (126 MHz, C_6D_6): δ = 200.76 (dt, $^1J(Rh,C)$ = 59.1 Hz, $^2J(P,C)$ = 9.9 Hz; *C*O), 169.49 (vt, $^2J(P,C)+^4J(P,C)$ = 17.0 Hz; C_{Ar}-O-P), 145.77 (dt, $^1J(Rh,C)$ = 25.9 Hz, $^2J(P,C)$ = 9.2 Hz; C_{ipso}), 128.29 (s; C_{Ar}-H), 104.63 (vt, $^3J(P,C)+^5J(P,C)$ = 13.4 Hz; C_{Ar}-H), 39.51 (vtd, $^1J(P,C)+^3J(P,C)$ = 16.6 Hz, $^2J(Rh,C)$ = 2.3 Hz; P*C*$(CH_3)_3$), 27.34 ppm (vt, $^2J(P,C)+^4J(P,C)$ = 8.0 Hz; $PC(CH_3)_3$); IR: $\tilde{\nu}_{CO}$ (CH_2Cl_2) = 1956 cm^{-1} (s); $\tilde{\nu}_{CO}$ (KBr) = 1948 cm^{-1} (s); $\tilde{\nu}_{CO}$ (film) = 1945 cm^{-1} (s); elemental analysis calcd (%) for $C_{23}H_{39}O_3P_2Rh$: C 52.28, H 7.44; found: C 52.44, H 7.36.

Formation of complex 15 by reaction of complex 17 with HBF_4: HBF_4·O-$(C_2H_5)_2$ (16.5 mg, 0.102 mmol) was added to a solution of **17** (10.0 mg, 0.019 mmol) in $CDCl_3$ (0.6 mL), and the resulting solution was stirred manually. See above for the full characterization of complex **15**.

Reaction of 3 with CH_3CN—in situ formation of complex 20: Complex **3** (23.8 mg, 0.043 mmol) was dissolved in $CDCl_3$ (0.55 mL). Then CH_3CN (3.0 mg, 0.073 mmol) was added. $^{31}P\{^1H\}$ NMR (162 MHz, $CDCl_3$, −30 °C): δ = 82.00 ppm (d, $^1J(Rh,P)$ = 96.1 Hz); ^1H NMR (400 MHz, $CDCl_3$, −30 °C): δ = 7.02 (d, $^3J(H,H)$ = 7.4 Hz, 2H; *meta* Ar-*H*), 6.92 (t, $^3J(H,H)$ = 7.4 Hz, 1H; *para* Ar-*H*), 3.50 (dvt, $^2J(H,H)$ = 16.9 Hz, $^2J(P,H)+^4J(P,H)$ = 6.0 Hz, 2H; Ar-CH_2-P, downfield part of ABX-system), 3.34 (dvt, $^2J(H,H)$ = 16.9 Hz, $^2J(P,H)+^4J(P,H)$ = 8.6 Hz, 2H; Ar-CH_2-P, upfield part of ABX-system), 2.49 (m, $^3J(H,H)$ = 6.9 Hz, 2H; P*C*$H(CH_3)_2$), 2.29 (s, 3H; coordinated CH_3CN), 2.28 (m, 2H; P*C*$H(CH_3)_2$, overlaps with CH_3CN signal), 1.30 (m, 12H; $PCH(CH_3)_2$), 1.14 (q, $^3J(H,H)$ = 6.7 Hz, 6H; $PCH(CH_3)_2$), 0.92 (q, $^3J(H,H)$ = 6.6 Hz, 6H; $PCH(CH_3)_2$), −15.80 ppm (dt, $^1J(Rh,H)$ = 23.8 Hz, $^2J(P,H)$ = 8.5 Hz, 1H; Rh-*H*); $^{13}C\{^1H\}$ NMR (101 MHz, $CDCl_3$, −30 °C): δ = 188.30 (dt, $^1J(Rh,C)$ = 43.5 Hz, $^2J(P,C)$ = 8.8 Hz; *C*O), 159.37 (dt, $^1J(Rh,C)$ = 23.9 Hz, $^2J(P,C)$ = 1.8 Hz; C_{ipso}), 146.86 (vt, $^2J(P,C)+^4J(P,C)$ = 16.4 Hz; Ar_{ortho}), 126.08 (s; Ar_{para}), 125.01 (d, $^2J(Rh,C)$ = 1.9 Hz; CH_3CN), 123.04 (vt, $^3J(P,C)+^5J(P,C)$ = 18.0 Hz; Ar_{meta}), 36.77 (vt, $^1J(P,C)+^3J(P,C)$ = 28.6 Hz; Ar*C*H_2P), 26.49 (vt, $^1J(P,C)+^3J(P,C)$ = 24.0 Hz; P*C*$H(CH_3)_2$), 24.43 (vtd, $^1J(P,C)+^3J(P,C)$ = 28.2 Hz, $^2J(Rh,C)$ = 1.3 Hz; P*C*$H(CH_3)_2$), 19.76 (s; $PCH(CH_3)_2$), 18.83 (s; $PCH(CH_3)_2$), 18.73 (s; $PCH(CH_3)_2$), 18.21 (s; $PCH(CH_3)_2$), 3.42 ppm (s; *C*H_3CN); ^{19}F NMR (376 MHz, $CDCl_3$, −30 °C): δ = −153.66 ppm (s; BF_4); $^{31}P\{^1H\}$ NMR (162 MHz, $CDCl_3$, 20 °C): δ = 81.83 ppm (br d, $^1J(Rh,P) \approx 80$ Hz); ^1H NMR (400 MHz, $CDCl_3$, 20 °C): δ = 7.03 (d, $^3J(H,H)$ = 7.2 Hz, 2H; *meta* Ar-*H*), 6.95 (m, 1H; *para* Ar-*H*), 3.52 (m, $^2J(H,H)$ = 16.7 Hz, 2H; Ar-CH_2-P, downfield part of ABX-system), 3.36 (m, $^2J(H,H)$ = 16.7 Hz, 2H; Ar-CH_2-P, upfield part of ABX-system), 2.50 (m, 2H; P*C*$H(CH_3)_2$), 2.28 (m, 2H; P*C*$H(CH_3)_2$), 2.10 (br s; free and coordinated CH_3CN), 1.31 (m, 12H; $PCH(CH_3)_2$), 1.17 (m, 6H; $PCH(CH_3)_2$), 0.97 (m, 6H; $PCH(CH_3)_2$), −15.89 ppm (br s, 1H; Rh-*H*); IR (2 % CH_3CN in CH_2Cl_2): $\tilde{\nu}_{CO}$ = 2063 cm^{-1} (s).

In situ preparation of ^{13}CO-labeled complex 20: Complex **3-^{13}CO** (4.8 mg, 0.009 mmol) was dissolved in CD_3CN (0.6 mL). $^{31}P\{^1H\}$ NMR (101 MHz, CD_3CN): δ = 79.24 ppm (dd, $^1J(Rh,P)$ = 96.1 Hz, $^2J(C,P)$ = 9.0 Hz); selected ^1H NMR (250 MHz, CD_3CN): δ = −15.79 ppm (m, $^1J(Rh,H)$ = 23.6 Hz, 1H; Rh-*H*); selected $^{13}C\{^1H\}$ NMR (63 MHz, CD_3CN): δ = 189.72 ppm (dt, $^1J(Rh,C)$ = 43.5 Hz, $^2J(C,P)$ = 9.0 Hz; *C*O).

Computational details: All calculations were carried out using the Gaussian 03 software package.[57] Geometry optimizations and evaluation of harmonic frequencies were performed at the density functional theory (DFT) level[58] using the PBE0 hybrid density functional[59] in conjunction with the SDB-cc-pVDZ basis set. This basis set is a combination of the Dunning cc-pVDZ basis set[60] for the main group elements and the Stuttgart–Dresden basis set RECP (relativistic energy-consistent pseudopotential)[61] for rhodium, with an added f-type polarization exponent taken as the geometric average of the two f exponents given by Martin and Sundermann.[62] The accuracy of the computational method in predicting the geometries of the experimental complexes was validated by calculating the geometries of complexes for which the crystal structures are known. All structures were fully optimized in the gas phase and characterized as minima or transition states by calculating the harmonic vibrational frequencies. The complete pathway for each reaction was traced by using the intrinsic reaction coordinate (IRC).[63] The IRC calculations were initiated from the optimized transition structure and followed the reaction pathway in the directions of the two energy minima connected by the pathway. Up to ten steps were used in each direction, with a step size of 0.1 $amu^{1/2}$bohr. The final structures were fully optimized to verify

the resulting minima. Basis set superposition errors (BSSE) were corrected by means of the counterpoise method.[64] Bulk solvent effects of the experimental chloroform or acetone media have been taken into account by means of the self-consistent reaction field (SCRF) method, using the continuum solvation model COSMO (conductor-like screening model) as it is implemented in Gaussian 03.[65] In this model, the solvent is represented by an infinite dielectric medium characterized by the relative dielectric constant of the bulk solvent ($\varepsilon = 4.9$ for chloroform and $\varepsilon = 20.7$ for acetone), and the effective cavity occupied by the solute in the solvent is calculated on the basis of the United Atom (UA0) topological model radii. Gas-phase optimized geometries were used in single-point calculations at the COSMO level. Dispersion interactions within the computed structures were also taken into account. These weak interactions, which are primarily determined by geometry, are usually poorly described by DFT methods, but can amount to 10–20 kcal mol^{-1} in large systems. In the present work, these interactions were included by adding an empirical dispersion correction term, as was proposed by Schwabe and Grimme,[66] with a value $s_6 = 0.67$.[67] Unless stated otherwise, energetic data are presented in this work as free energy changes (ΔG) at 298.15 K or as binding energies ($= -\Delta G_{298}$), and include corrections for solvation and dispersion. For qualitative interpretation of the computational results, electron density of the complexes in optimized geometries was analyzed using natural bond orbital (NBO) and natural population analysis (NPA),[68] charge decomposition analysis (CDA)[69] and molecular orbital overlap population (MOOP) analysis.[70] Atomic polar tensor (APT) charges[71] were determined from the analytical second derivatives (vibrational frequencies) calculations.

CCDC-734773 (**6**), 734774 (**14**), 734775 (**16**), and 734776 (**17**) contain the supplementary crystallographic data for this paper. These data can be obtained free of charge from The Cambridge Crystallographic Data Centre via www.ccdc.cam.ac.uk/data_request/cif.

Acknowledgements

This research was supported by the Israel Science Foundation, the Petroleum Research Fund (administered by ACS), and the Kimmel Center for Molecular Design. D.M. is the holder of the Israel Matz Professorial Chair. The authors would like to thank the referees of this manuscript for their valuable comments.

[1] a) B. A. Arndtsen, R. G. Bergman, T. A. Mobley, T. H. Peterson, *Acc. Chem. Res.* **1995**, *28*, 154–162; b) A. E. Shilov, G. B. Shul′pin, *Chem. Rev.* **1997**, *97*, 2879–2932; c) J. A. Labinger, J. E. Bercaw, *Nature* **2002**, *417*, 507–514; d) *Activation and Functionalization of C–H Bonds* (Eds.: K. I. Goldberg, A. S. Goldman), ACS, Washington, **2004**; e) S. Sakaki, *Top. Organomet. Chem.* **2005**, *12*, 31–78.

[2] It must be stressed that the two-electron oxidation of the metal center, as implied for most cases of oxidative addition, is strictly a formal notion. In reality, the M–H and M–C bonds resulting from C–H oxidative addition have substantial covalent character, and hence only partial electron transfer takes place.

[3] a) C. Hall, R. N. Perutz, *Chem. Rev.* **1996**, *96*, 3125–3146; b) R. H. Crabtree, *J. Organomet. Chem.* **2004**, *689*, 4083–4091.

[4] J.-Y. Saillard, R. Hoffmann, *J. Am. Chem. Soc.* **1984**, *106*, 2006–2026.

[5] a) K. Tatsumi, R. Hoffmann, A. Yamamoto, J. K. Stille, *Bull. Chem. Soc. Jpn.* **1981**, *54*, 1857–1867; b) F. Ozawa in *Current Methods in Inorganic Chemistry, Vol. 3* (Eds.: H. Kurosaw, A. Yamamoto), Elsevier, Amsterdam, **2003**, pp. 479–512.

[6] a) M.-D. Su, S.-Y. Chu, *Inorg. Chem.* **1998**, *37*, 3400–3406; b) M.-D. Su, S.-Y. Chu, *J. Phys. Chem. A* **1998**, *102*, 10159–10166.

[7] M. Montag, L. Schwartsburd, R. Cohen, G. Leitus, Y. Ben-David, J. M. L. Martin, D. Milstein, *Angew. Chem.* **2007**, *119*, 1933–1936; *Angew. Chem. Int. Ed.* **2007**, *46*, 1901–1904.

[8] The hydride ligand in complex **6** was explicitly located in the electron-density map.

[9] The crystal structure of complex **6** exhibits partial disorder with respect to the acetone ligand, the *tert*-butyl substituents on P2 and the BF_4^- counterion. Nonetheless, this disorder does not significantly alter the primary coordination sphere of rhodium.

[10] All ^{1}H NMR signals of complex **6**, other than the hydride signal, are relatively insensitive to the solvent, with $|\Delta\delta| \leq 0.16$ ppm for chloroform and acetone.

[11] a) A. Vigalok, O. Uzan, L. J. W. Shimon, Y. Ben-David, J. M. L. Martin, D. Milstein, *J. Am. Chem. Soc.* **1998**, *120*, 12539–12544; b) A. Vigalok, B. Rybtchinski, L. J. W. Shimon, Y. Ben-David, D. Milstein, *Organometallics* **1999**, *18*, 895–905.

[12] This strategy was also employed in the characterization of complex **4**, as described in ref. [7].

[13] Partridge et al. have studied the ^{1}H,^{13}C coupling constants in octahedral aryl–hydrido–carbonyl Rh^{III} complexes. They have found that the magnitude of ^2J(C,H) for the carbonyl and hydride ligands in these systems is very large for the *trans* configuration (e.g., 65 Hz), but small for the *cis* configuration (e.g., 4.7 Hz). For further details, see: M. G. Partridge, B. A. Messerle, L. D. Field, *Organometallics* **1995**, *14*, 3527–3530.

[14] A very small ^2J(C,C) value is expected for carbonyl ligands in the *cis* configuration. For a previous example, see: A. Silvio, O. Domenico, *J. Chem. Soc. Chem. Commun.* **1981**, 300–302.

[15] It is interesting to note that when the dichloromethane solution containing complexes **7** and **8** was warmed from −60 °C to room temperature, the NMR signals for complex **7** were found to be very broad (e.g., $\Delta\nu_{1/2} \approx 110$ Hz for the ^{31}P{^{1}H} signal), in contrast to the sharp signals observed at room temperature before the solution had been cooled to −60 °C. These broad signals slowly narrowed as the sample was allowed to stand at room temperature (e.g., after 10 min the ^{31}P{^{1}H} signal gave $\Delta\nu_{1/2} \approx 40$ Hz). These line-shape changes probably originate from the relatively slow release of CO from complex **8**, for which the rate is roughly on the timescale of the NMR spectroscopy experiment at the applied magnetic field (9.4 T, 400 MHz).

[16] Under the experimental conditions employed in this work, the signal for the agostic proton in **7** appeared at about $\delta = 4.0$ ppm, which is about 13 ppm downfield from the hydride signal. This large difference in resonance frequencies insures that the agostic proton is not affected by the selective saturating pulses used to irradiate the hydride ligand.

[17] In general, chlorohydrocarbons, including chloroform, are very weak ligands. For a recent report quantifying the relative binding constants of simple chlorohydrocarbons, see: D. M. Tellers, R. G. Bergman, *J. Am. Chem. Soc.* **2001**, *123*, 11508–11509.

[18] Although no spectroscopic evidence for the coordination of BF_4^- was observed, its interaction with the cationic complexes cannot be completely neglected. The role of the counterion will be further discussed below.

[19] Preliminary results of this study have already appeared in our previous report (see ref. [7]). However, our previous computational results were based on structural optimizations with a relatively small basis set (SDD), followed by single-point energy calculations using a larger basis set (SDB-cc-pVDZ). In the present work, the basis set SDB-cc-pVDZ was used for both structure and energy calculations, thereby providing more accurate results.

[20] It should be borne in mind that the formation of the aryl–hydrido complexes is counteracted by the low solubility of CO in chloroform (≈8 μM at 1 atm and 25 °C; data adapted from R. W. Cargill, *Wiley Solubility Data Series, Vol. 43*, Wiley, New York, **1990**, p. 246–247). This low solubility, and the ability of CO to escape from the solution, drives the equilibrium to the reactant side. This probably accounts for the fact that the *t*Bu-substituted aryl–hydrido complex was not observed at room temperature, as our DFT results suggest that it is only slightly more stable than its agostic precursor.

[21] The complex $[Rh(acetone)_2(CO)_2]BF_4$ was prepared in situ by chloride abstraction from the neutral dimer $[\{Rh(CO)_2Cl\}_2]$ in acetone. This solvent was used instead of chloroform, since the complex is

unstable in weakly coordinating solvents. See the Experimental Section for more details.

[22] The byproducts observed upon reaction of $[Rh(acetone)_2(CO)_2]BF_4$ with either ligand **1** or **5** were not observed when agostic complexes **3** and **7** were treated with CO at low temperatures.

[23] The metal center and hydride ligand/agostic proton represent the two most electrophilic sites in the examined complexes. Therefore, these moieties are the most likely to participate in direct interactions with the BF_4^- counterion.

[24] The weak binding of the BF_4^- counterion renders the potential-energy surface very flat near the saddle point associated with the transition state. This prevented us from locating transition states in the *t*Bu-substituted systems, wherein the anion is located in the second coordination sphere. The energies of **TS**(**7**–**11**)-BF_4^H and **TS**-(**12**–**8**)-BF_4^H were estimated using relaxed scans of the potential-energy surface near the critical point.

[25] a) I. Göttker-Schnetmann, P. White, M. Brookhart, *J. Am. Chem. Soc.* **2004**, *126*, 1804–1811; b) I. Göttker-Schnetmann, P. S. White, M. Brookhart, *Organometallics* **2004**, *23*, 1766–1776; c) I. Göttker-Schnetmann, M. Brookhart, *J. Am. Chem. Soc.* **2004**, *126*, 9330–9338; d) A. S. Goldman, A. H. Roy, Z. Huang, R. Ahuja, W. Schinski, M. Brookhart, *Science* **2006**, *312*, 257–261; e) W. H. Bernskoetter, M. Brookhart, *Organometallics* **2008**, *27*, 2036–2045.

[26] The hydride ligand in complex **14** was explicitly located in the electron-density map.

[27] The slight difference observed in the $^{13}C,^{31}P$ coupling constants of the reaction products obtained by treating complex **14** with either regular or ^{13}C-labeled CO was attributed to the presence of varying concentrations of acetone in the reaction mixtures. This residual acetone, which originates from complex **14** itself, was found to coordinate to the metal center of the reaction product (see below), thereby altering its NMR spectra. See the main text and ref. [28] for further details.

[28] For example, when a 6 mM solution of **14** in $CDCl_3$ was used to prepare complex **15**, the latter gave rise to a hydride signal at $\delta = -14.98$ ppm (at $-40\,^\circ C$), but when a 90 mM solution was used, the same signal appeared at $\delta = -12.36$ ppm (at the same temperature). The other ^1H NMR signals of complex **15** were found to be relatively insensitive to changes in complex concentration, with $|\Delta\delta| \leq 0.06$ ppm for 6 and 90 mM. The observed changes in the hydride signal reflect the increased binding of acetone, the concentration of which increases with that of the parent complex **14**. This effect was clearly demonstrated by treating a 6 mM solution of **14** in chloroform with CO in the presence of an intentionally added 100-fold excess of acetone, and comparing the ^1H NMR spectrum of the afforded complex **15** to that of a similarly prepared sample containing no added acetone. The hydride signal of **15** appeared at $\delta = -12.76$ ppm ($^2J(Rh,H) = 40.0$ Hz) in the presence of excess acetone, and at $\delta = -14.94$ ppm ($^2J(Rh,H) = 43.5$ Hz) in its absence. These results also point to slight changes in the NMR spectroscopy coupling constants observed for atoms in the first coordination sphere of **15** (e.g., hydride $^2J(Rh,H)$ and carbonyl $^1J(Rh,C)$ and $^2J(P,C)$), all of which are due to acetone coordination.

[29] The product obtained by the reaction of **15** with CO, although isolable at room temperature, was found to decompose at this temperature over the time period required to record the ^{13}C NMR spectrum. Therefore, a low temperature measurement was employed.

[30] The best representative polymorph list of the Cambridge Structural Database (CSD, version 5.29) was found to contain 1063 complexes of rhodium with terminal CO ligands, for which the *R* factor $\leq 10\,\%$. The average C–O bond length for the CO ligands in these complexes is (1.139 ± 0.024) Å, and the average Rh–C bond for these ligands is (1.858 ± 0.046) Å.

[31] G. Herzberg, *Molecular Spectra and Molecular Structure*; Van Nostrand Reinhold, New York, **1966**.

[32] For a recent analysis of C–O and metal–C bond lengths in metal carbonyls, see: R. K. Hocking, T. W. Hambley, *Organometallics* **2007**, *26*, 2815–2823.

[33] The asymmetric unit for complex **16** contains two BF_4 anions, one of which originates from HBF_4. See the main text for more details.

[34] a) M. L. Kuznetsov, *Russ. Chem. Rev.* **2002**, *71(4)*, 265–282; b) M. L. Kuznetsov, *THEOCHEM* **2004**, *674*, 33–42.

[35] The aryl–hydrido complex **20** is computed to be slightly less stable than agostic complex **3**. This stands in contradiction to the experimental findings, which indicate that **20** is more stable than **3**, since the former was obtained quantitatively when a small excess of acetonitrile was added to **3**. As above, this discrepancy is partially resolved by explicitly including the BF_4^- counterion in the calculations. With counterion interaction energies of 4.8 and 7.2 kcal mol^{-1} at 25 and $-40\,^\circ C$, respectively, complex **20**-BF_4 is less stable than **3**-BF_4 by only 2.7 and 0.1 kcal mol^{-1}, respectively.

[36] M. Brookhart, M. L. H. Green, G. Parkin, *Proc. Natl. Acad. Sci. USA* **2007**, *104*, 6908–6914.

[37] a) M. E. van der Boom, M. A. Iron, O. Atasoylu, L. J. W. Shimon, H. Rozenberg, Y. Ben-David, L. Konstantinovski, J. M. L. Martin, D. Milstein, *Inorg. Chim. Acta* **2004**, *357*, 1854–1864; b) B. Rybtchinski, R. Cohen, Y. Ben-David, J. M. L. Martin, D. Milstein, *J. Am. Chem. Soc.* **2003**, *125*, 11041–11050; c) P. Yang, I. Warnke, R. L. Martin, P. J. Hay, *Organometallics* **2008**, *27*, 1384–1392.

[38] E. Clot, O. Eisenstein, *Struct. Bonding (Berlin)* **2004**, *113*, 1–36.

[39] G. J. Kubas, *Catal. Lett.* **2005**, *104*, 79–101.

[40] M. Montag, I. Efremenko, R. Cohen, G. Leitus, L. J. W. Shimon, Y. Diskin-Posner, Y. Ben-David, J. M. L. Martin, D. Milstein, *Chem. Eur. J.* **2008**, *14*, 8183–8194.

[41] The involvement of aromatic π orbitals is particularly important in the weakly agostic intermediates **10**, **12**, and **22**, all of which exhibit long Rh–C_{ipso} (2.5–2.7 Å) and Rh–H (2.3–2.6 Å) bonds. These complexes are also characterized by a relatively modest activation of the C_{ipso}–H bond ($WBI_{C-H} > 0.8$), as well as a relatively small angle between the Rh atom and the plane of the aromatic ring (114–120°).

[42] The extent of arene bending is directly related to the strength of the interaction, that is, the stronger the interaction between the metal and aromatic system, the more pronounced the bending of the ring will be.

[43] A clear link between arene bending and C–H bond activation is evident from the optimized structures of agostic complexes **3**, **7**, **19**, and **20**. These complexes exhibit obtuse angles between rhodium and the aromatic ring (138–156°), and these are associated with activated C–H bonds ($WBI_{C-H} = 0.68$–0.74), as well as relatively short Rh–C (2.1–2.3 Å) and Rh–H (1.9–2.0 Å) bond lengths. Moreover, these complexes are characterized by higher acidities of the agostic hydrogen atoms relative to the weakly agostic intermediates **10**, **12**, and **22**, as reflected by the computed atomic polar tensor (APT) charges on the agostic hydrogen atoms. Thus, the APT charges for complexes **3**, **7**, **19**, and **20** are in the range of 0.17–0.28, while those for **10**, **12**, and **22** are only 0.07–0.08. In general, comparison of the results obtained in the present work with previous studies of agostic arene complexes (ref. [11a], [37a], and [37b]) indicates that, independent of the transition metal and ligand environment, a larger angle between the metal and aromatic ring corresponds to higher C–H bond activation, as well as enhanced acidity of the hydrogen atom.

[44] Although kinetically possible, the deprotonation of complex **19** is calculated to be endothermic by 3.6 kcal mol^{-1}. It is probable that under the experimental conditions—in particular the relatively low concentration of reactants—this reaction is driven by entropic effects.

[45] B. Windmüller, O. Nürnberg, J. Wolf, H. Werner, *Eur. J. Inorg. Chem.* **1999**, 613–619. The procedure was modified by using $AgBF_4$ instead of $AgPF_6$ and conducting the whole process at room temperature.

[46] D. G. Gusev, M. Madott, F. M. Dolgushin, K. A. Lyssenko, M. Yu. Antipin, *Organometallics* **2000**, *19*, 1734–1739.

[47] L. J. Farrugia, *J. Appl. Crystallogr.* **1997**, *30*, 565.

[48] Cambridge Structural Database (CSD; version 5.29), Cambridge Crystallographic Data Centre, 12 Union Road, Cambridge, England, **2007**.

[49] F. H. Allen, *Acta Crystallogr. Sect. B* **2002**, *58*, 380–388.
[50] I. J. Bruno, J. C. Cole, P. R. Edgington, M. Kessler, C. F. Macrae, P. McCabe, J. Pearson, R. Taylor, *Acta Crystallogr. Sect. B* **2002**, *58*, 389–397.
[51] CCDC Vista—A Program for the Analysis and Display of Data Retrieved from the CSD, Cambridge Crystallographic Data Centre, 12 Union Road, Cambridge, England, **1994**.
[52] J. van de Streek, *Acta Crystallogr. Sect. B* **2006**, *62*, 567–579.
[53] Z. Otwinowski, W. Minor, *Methods Enzymol.* **1997**, *276*, 307–326.
[54] G. M. Sheldrick, *Acta Crystallogr. Sect. A* **2008**, *64*, 112–122.
[55] A. Altomare, M. C. Burla, M. Camalli, G. L. Cascarano, C. Giacovazzo, A. Guagliardi, A. G. G. Moliterni, G. Polidori, R. Spagna, *J. Appl. Crystallogr.* **1999**, *32*, 115–119.
[56] The considerable differences between the NMR chemical shifts for the ^{13}CO-labeled complex **15**, relative to the nonlabeled complex, are due to differences in sample concentration. Due to technical constraints, the solution containing the labeled complex was approximately 10 times more dilute than that of the nonlabeled complex. See the main text for further details regarding the effect of complex concentration on the NMR spectra.
[57] Gaussian 03, Revision E.01, M. J. Frisch, G. W. Trucks, H. B. Schlegel, G. E. Scuseria, M. A. Robb, J. R. Cheeseman, J. A. Montgomery, Jr., T. Vreven, K. N. Kudin, J. C. Burant, J. M. Millam, S. S. Iyengar, J. Tomasi, V. Barone, B. Mennucci, M. Cossi, G. Scalmani, N. Rega, G. A. Petersson, H. Nakatsuji, M. Hada, M. Ehara, K. Toyota, R. Fukuda, J. Hasegawa, M. Ishida, T. Nakajima, Y. Honda, O. Kitao, H. Nakai, M. Klene, X. Li, J. E. Knox, H. P. Hratchian, J. B. Cross, V. Bakken, C. Adamo, J. Jaramillo, R. Gomperts, R. E. Stratmann, O. Yazyev, A. J. Austin, R. Cammi, C. Pomelli, J. W. Ochterski, P. Y. Ayala, K. Morokuma, G. A. Voth, P. Salvador, J. J. Dannenberg, V. G. Zakrzewski, S. Dapprich, A. D. Daniels, M. C. Strain, O. Farkas, D. K. Malick, A. D. Rabuck, K. Raghavachari, J. B. Foresman, J. V. Ortiz, Q. Cui, A. G. Baboul, S. Clifford, J. Cioslowski, B. B. Stefanov, G. Liu, A. Liashenko, P. Piskorz, I. Komaromi, R. L. Martin, D. J. Fox, T. Keith, M. A. Al-Laham, C. Y. Peng, A. Nanayakkara, M. Challacombe, P. M. W. Gill, B. Johnson, W. Chen, M. W. Wong, C. Gonzalez, J. A. Pople, Gaussian, Inc., Wallingford CT, **2004**.
[58] a) W. Kohn, L. J. Sham, *Phys. Rev.* **1965**, *140*, A1133–A1138; b) R. G. Parr, W. Yang, *Density Functional Theory of Atoms and Molecules*, Oxford University Press, New York, **1970**, p. 230.
[59] C. Adamo, M. Cossi, V. Barone, *J. Mol. Struct.* **1999**, *493*, 145–157.
[60] T. H. Dunning, Jr., *J. Chem. Phys.* **1989**, *90*, 1007–1023.
[61] T. H. Dunning Jr., P. J. Hay, *Modern Theoretical Chemistry, Vol. 3*, Plenum, New York, **1976**, Chapter 1.
[62] J. M. L. Martin, A. Sundermann, *J. Chem. Phys.* **2001**, *114*, 3408–3420.
[63] C. Gonzalez, H. B. Schlegel, *J. Phys. Chem.* **1990**, *94*, 5523–5527.
[64] a) S. F. Boys, F. Bernardi, *Mol. Phys.* **1970**, *19*, 553–566; b) S. Simon, M. Duran, J. J. Dannenberg, *J. Chem. Phys.* **1996**, *105*, 11024–11031.
[65] a) A. Klamt, G. Schüürmann, *J. Chem. Soc. Perkin Trans. 2* **1993**, 799–805; b) V. Barone, M. Cossi, *J. Phys. Chem. A* **1998**, *102*, 1995–2001.
[66] a) T. Schwabe, S. Grimme, *Phys. Chem. Chem. Phys.* **2007**, *9*, 3397–3406; b) T. Schwabe, S. Grimme, *Acc. Chem. Res.* **2008**, *41*, 569–579.
[67] A. Karton, A. Tarnopolsky, J.-F. Lamère, G. C. Schatz, J. M. L. Martin, *J. Phys. Chem. A* **2008**, *112*, 12868–12886.
[68] a) J. P. Foster, F. Weinhold, *J. Am. Chem. Soc.* **1980**, *102*, 7211–7218; b) A. E. Reed, L. A. Curtiss, F. Weinhold, *Chem. Rev.* **1988**, *88*, 899–926.
[69] S. Dapprich, G. Frenking, *J. Phys. Chem.* **1995**, *99*, 9352–9362.
[70] a) R. Hoffmann, *Solids and Surfaces: A Chemist's View of Bonding in Extended Structures,* VCH, Weinheim, **1988**, pp. 42–55; b) GaussSum 1.0, N. M. O'Boyle, Dublin City University, **2005**. Available at http://gausssum.sourceforge.net.
[71] J. Cioslowski, *J. Am. Chem. Soc.* **1989**, *111*, 8333–8336.

Received: June 5, 2009
Published online: November 13, 2009

